

AD-A050 257

ARMY MISSILE RESEARCH AND DEVELOPMENT COMMAND REDSTO--ETC F/6 9/1
SUPPORT OF MX ELECTROMAGNETIC PULSE VALIDATION, INTERIM REPORT.(U)
JUN 77 D MATHEWS

UNCLASSIFIED

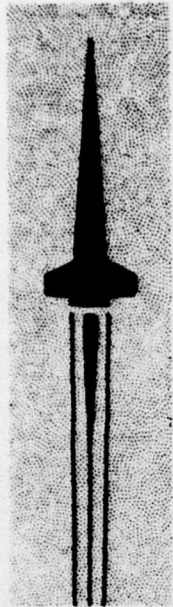
DRDRI-EA-77-5

NL

1 OF 1
AD
A050257



AD A 050257



2

TECHNICAL REPORT EA-77-5

SUPPORT OF MXELECTROMAGNETIC PULSE
VALIDATION, INTERIM REPORT

**U.S. ARMY
MISSILE
RESEARCH
AND
DEVELOPMENT
COMMAND**

David Mathews
Advanced Systems Development and Manufacturing
Technology Directorate

June 1977



Redstone Arsenal, Alabama 35809

Approved for public release; distribution unlimited.

DDC
RECEIVED
FEB 21 1978
D

DISPOSITION INSTRUCTIONS

**DESTROY THIS REPORT WHEN IT IS NO LONGER NEEDED. DO NOT
RETURN IT TO THE ORIGINATOR.**

DISCLAIMER

**THE FINDINGS IN THIS REPORT ARE NOT TO BE CONSTRUED AS AN
OFFICIAL DEPARTMENT OF THE ARMY POSITION UNLESS SO DESIGNATED BY OTHER AUTHORIZED DOCUMENTS.**

TRADE NAMES

**USE OF TRADE NAMES OR MANUFACTURERS IN THIS REPORT DOES
NOT CONSTITUTE AN OFFICIAL INDORSEMENT OR APPROVAL OF
THE USE OF SUCH COMMERCIAL HARDWARE OR SOFTWARE.**

UNCLASSIFIED

SECURITY CLASSIFICATION OF THIS PAGE (When Data Entered)

REPORT DOCUMENTATION PAGE		READ INSTRUCTIONS BEFORE COMPLETING FORM
1. REPORT NUMBER EA-77-5 ✓	2. GOVT ACCESSION NO.	3. RECIPIENT'S CATALOG NUMBER
4. TITLE (and Subtitle) SUPPORT OF XX ELECTROMAGNETIC PULSE VALIDATION, INTERIM REPORT.	5. TYPE OF REPORT AND PERIOD COVERED Technical Report	
6. AUTHOR(s) David Mathews	7. PERFORMING ORG. REPORT NUMBER EA-77-5	
8. PERFORMING ORGANIZATION NAME AND ADDRESS Commander US Army Missile Research and Development Command Attn: DRDMI-EA Redstone Arsenal, Alabama 35809	9. CONTRACT OR GRANT NUMBER(s) DRDMI-EA-77-5	
10. PROGRAM ELEMENT, PROJECT, TASK AREA & WORK UNIT NUMBERS AMCMS 696000.0000722	11. CONTROLLING OFFICE NAME AND ADDRESS Commander US Army Missile Research and Development Command Attn: DRDMI-TI Redstone Arsenal, Alabama 35809	
12. MONITORING AGENCY NAME & ADDRESS (if different from Controlling Office)	13. REPORT DATE June 1977	
	14. NUMBER OF PAGES 74	
	15. SECURITY CLASS. (of this report) UNCLASSIFIED	
16. DISTRIBUTION STATEMENT (of this Report) DISTRIBUTION STATEMENT A Approved for public release; Distribution Unlimited		
17. DISTRIBUTION STATEMENT (of the abstract entered in Block 20, if different from Report) Approved for public release; distribution unlimited.		
18. SUPPLEMENTARY NOTES		
19. KEY WORDS (Continue on reverse side if necessary and identify by block number) Second breakdown Submicrosecond pulse effects Junction bipolar devices Construction defects Transistors Geometrical and structural effects Integrated circuits Silicon on sapphire diodes Nondestructive screening techniques Self-heating		
20. ABSTRACT (Continue on reverse side if necessary and identify by block number) This interim report outlines the technical progress to date on the Electrical Overstress Program at the US Army Missile Research and Development Command. The program is aimed at providing a better theoretical model of the physics of second breakdown in junction bipolar diodes, transistors, and integrated circuits, and applying this information in the development of nondestructive screening techniques for eliminating device types and individual		

ABSTRACT (CONTINUED)

DD FORM 1 JAN 75 1473 EDITION OF 1 NOV 65 IS OBSOLETE

UNCLASSIFIED

SECURITY CLASSIFICATION OF THIS PAGE (When Data Entered)

410398

elf

UNCLASSIFIED

SECURITY CLASSIFICATION OF THIS PAGE (When Data Entered)

ABSTRACT (CONTINUED)

samples which are especially susceptible to high power pulses. The program features a continuation of Defense Nuclear Agency funded research using special silicon on sapphire diodes in which the effects of self-heating are directly observable, computer analysis and simulation of both conventional transistor and special silicon on sapphire diode behavior, and selection and measurement of electrical parameters required for prediction of overstress susceptibility.

ACCESSION FOR	
NTIS	White Section <input checked="" type="checkbox"/>
DDP	Dark Section <input type="checkbox"/>
UNANNOUNCED	<input type="checkbox"/>
JUSTIFICATION	
BY	
DISTRIBUTION/AVAILABILITY CODES	
Dist.	AVAIL. and/or SPECIAL
A	

DDC
RECEIVED
FEB 21 1978
D

UNCLASSIFIED

SECURITY CLASSIFICATION OF THIS PAGE (When Data Entered)

CONTENTS

	Page
I. INTRODUCTION	3
II. TYPES OF SECOND BREAKDOWN	6
III. SECOND BREAKDOWN	25
IV. MELT CHANNEL FORMATION AFTER SECOND BREAKDOWN	39
V. CURRENT MODE SECOND BREAKDOWN	60
REFERENCES	69

I. INTRODUCTION

This interim report outlines the technical progress to date on the Electrical Overstress Program at the US Army Missile Research and Development Command (MIRADCOM), sponsored by Defense Nuclear Agency (DNA), SAMSO (MNNH), and MIRADCOM, and provides a brief outline of the background, plans, etc. The program is aimed at providing a better theoretical model of the physics of second breakdown in junction bipolar diodes, transistors, and integrated circuits, and applying this information in the development of nondestructive screening techniques for eliminating device types and individual samples which are especially susceptible to high power pulses. Particular subjects of interest in FY77 include short (submicrosecond) pulse effects, importance of various construction defects, geometrical and structural effects, and applicability of existing information to screening. The program features a continuation of DNA funded research using special silicon on sapphire (SOS) diodes in which the effects of self-heating are directly observable, computer analysis and simulation of both conventional transistor and special SOS diode behavior, and selection and measurement of electrical parameters required for prediction of overstress susceptibility.

Efforts currently under way include contractor efforts in updating and automating SOS diode test facilities, analysis of anomalous short pulse (nanosecond time regime) effects, generalizing and "speeding up" an existing computer code for second breakdown simulation, design and fabrication of new SOS diode samples, development of a quantitative physical model for filament formation, and application of existing data to an improved engineering-accuracy prediction technique for failure levels in conventional transistors. Because these efforts have only recently begun, results are of such a preliminary nature that it does not appear advisable to report them at this time. The work discussed in this report is thus an integration of previous research (primarily by these contractors) and current in-house efforts. The in-house work is meant to provide approximate solutions to various problems which enter into analysis of second breakdown, so that these solutions can serve as a starting point for more sophisticated numerical analyses. Factors considered thus far include carrier avalanche (first breakdown), geometrical effects, self-heating, and normal transistor action; only silicon devices are considered; and conditions under which tunneling might occur are excluded.

Second breakdown will be taken here to mean the transition from uniform to nonuniform conduction in junction bipolar devices. It will include the development of filamentation (current constriction), but not damage. Extremes of operation, e.g., very short or very long driving pulses, may cause thermal effects to be negligible or to dominate, but in general, the process must include both thermal and electrical effects.

A number of phenomena are demonstrated which fit the second breakdown criterion of producing a sudden drop in the voltage across a pn junction which is driven by a pulsed constant current source. These phenomena include nonlinear heating, change in the sign of the slope of the resistivity-temperature curve, self-biasing due to lateral current flow (current mode), and melt channel formation. The latter is excluded so that the definition can be further restricted to a nondestructive process. Effects of nuclear radiation have not yet been considered (the so-called synergistic effects), but will be included in later computer programming.

It has been noted, in agreement with theories of a critical temperature or a critical energy, that when reverse biasing current pulses of less than a few milliseconds in duration are used as the driving source, the hot spots always begin in the avalanching depletion region. For this reason, a large portion of the work has been directed toward determining the physical location where first breakdown would occur. A need for information on sustaining voltages for nonplanar structures was clearly indicated. Previous work by many authors had already indicated that hot spots normally form in avalanche regions, but not necessarily at the point of maximum electric field as calculated from the geometry of the device. As shown schematically in Figure 1, variations in the geometrical dimensions of a given device may be sufficient to cause avalanche breakdown to occur in entirely different locations in nominally the same device [1]. This has important consequences for second breakdown, because avalanche is usually the first step in the sequence starting with application of the transient signal, passing through second breakdown, and ending in damage. One sample may be nearly impossible to damage in a given circuit configuration, while a second will be extremely susceptible to damage. It is important to note that while second breakdown, in the reverse-bias case, begins in an avalanching region, the location of the second breakdown site seldom coincides with the location of maximum field. Microstructural defects have been proposed by some authors as the explanation of this situation, because they could account for local high field concentrations. Other authors disagree. A large local electric field could be located at or near the hot spot if a microstructural inhomogeneity existed. Budenstein, et al. [2] have shown by calculation that the effect of an inhomogeneity is to shift the hot spot location from its geometrically predicted site to an intermediate location between the site of the inhomogeneity and the geometrically predicted site. Thus, a submicroscopic examination of the new hot spot site would probably show nothing out of the ordinary. Moreover, the hot spot locations are known to vary with the amplitude of the driving pulse. Any attempt to correlate the presence of an inhomogeneity with an externally-measured electrical parameter should be expected to require driving the device into avalanche, because the inhomogeneity may very well be dormant as far as electrical activity is concerned until the avalanche condition is reached. For example, conditions required for the generation of certain types of electrical noise might include driving the device into heavy avalanche.

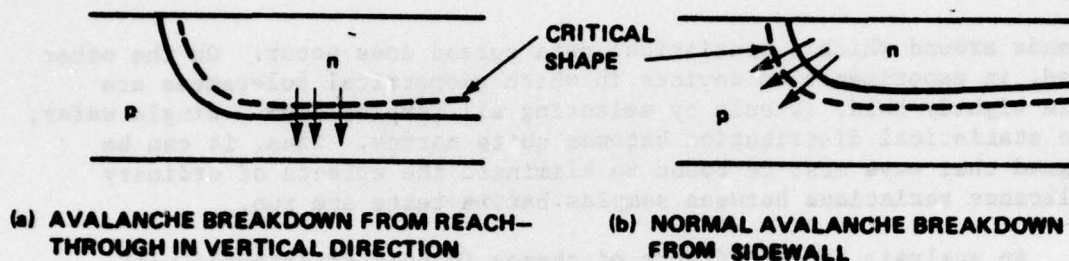


Figure 1. Cross section of devices with nearly the same dimensions.

SOS diodes have already proved to be an extremely effective tool in studying second breakdown. It should not be expected that the results of analyses of SOS diodes will carry over to conventional transistors, but rather that the SOS diodes should act as a proving ground for the analytical tools developed for the study of conventional devices. For example, the heat flow patterns in the depletion region of an SOS diode are vastly different than those in the depletion region of an epitaxial planar device, but the same general equations are used in each case. Some problems do exist with SOS diodes. Surface and interface states are important factors in determining avalanche breakdown of the samples [3]. This complicates the analysis and leads to conditions unlike those found in conventional transistors. Other bulk effects may be overshadowed by surface effects. The avalanche voltages predicted by SOS diode analysis are greater than those seen experimentally. The extensive series resistance regions tend to mask some purely junction effects and overemphasize bulk properties. The most serious limitation is that except for electrical characteristics, only changes in temperature may be observed. Thus, injection effects can only be observed indirectly. However, it is important to realize that every major, and nearly every minor, observation of second breakdown effects in SOS diodes has been found to have a counterpart in conventional devices.*

An analysis along the lines of the Wunsch model will be given for very high amplitude pulses of current (and therefore short delay times), predicting the experimentally-observed inverse relation between delay time and applied power. Neither this model nor the Wunsch model for lower amplitude pulses, though both are derived from the heat equation, provides a physical explanation for the observed or critical temperature. Implicit in both models is the assumption that only geometrical effects are important, not statistically-based microstructural defects. Examination of experimental data shows that the two models predict general

*Dr. P. P. Budenstein, private communication, March 1977.

trends around which a statistical data spread does occur. On the other hand, in experiments on devices in which geometrical tolerances are more tightly held, if only by selecting all samples from a single wafer, the statistical distribution becomes quite narrow. Thus, it can be argued that ways must be found to eliminate the effects of ordinary tolerance variations between samples before tests are run.

An analysis of the effects of change in bulk resistivity with temperature will be given. This indicates that the voltage drop across the high resistivity side can occur quite rapidly. While this effect is probably negligible in most cases in conventional devices, because the device must heat sufficiently to cross over the resistivity-temperature "hump" while maintaining a reasonably large undepleted collector region, it is important to the understanding of SOS device phenomena.

The melt analysis of Budenstein, et al. [2] is repeated, using an approximation technique and completely different boundary conditions. The two models can be shown under certain circumstances to have the same general form, but the relative importance of heat loss and melting terms can be vastly different. The analysis here assumes that the melt channel does not stop growing before its diameter becomes comparable to the thickness of the silicon layer but reaches a ribbon-like state and then stops growing. Depending on actual physical data, the channel can still stop while cylindrical. Good data on the thermal properties of molten silicon do not appear to exist. Some estimates can be made by working back from curve fits of laboratory data to the theoretical equations. Even thermal data below the melting point of silicon show a wide spread. This will undoubtedly remain a problem when more sophisticated numerical analyses are performed.

Finally, it seems appropriate to stress the preliminary nature of these results and to point out that many of the authors cited in this report disagree strongly with each other's interpretations of the data presented here.

II. TYPES OF FIRST BREAKDOWN

Avalanche breakdown in pn junctions is a subject which appears in essentially every text on semiconductor device physics, but its treatment is usually rather sketchy. Moreover, the solution for cartesian, or rectangular, coordinates is the only one discussed, and the sustaining voltage, which depends on a limited avalanche, is seldom considered; however, there are the exceptions [1, 4, and 5]. Following Gärtner [6], the discussion here will begin with the continuity equations. In each device, the volume of the pn junction depletion region can usually be approximated by considering it to be made up of subvolumes in the shape of rectangular parallelepipeds, quarter segments

of cylinders, and eighth segments of spheres (Figures 2, 3, 4, and 5). Symmetry then allows these volumes to be treated one-dimensionally in the appropriate coordinate system, because the current density vector has a single component. Each subvolume considered will be referred to by its coordinate system: cartesian, cylindrical, spherical. Because the boundary conditions and internal characteristics (doping density, etc.) will not, in general, be the same for each subvolume, first breakdown will occur in one location at a lower applied voltage than in all the others. A comparison of the breakdown of all the subvolumes thus yields the first breakdown. Analysis is greatly simplified if total carrier currents rather than the corresponding current densities are used.

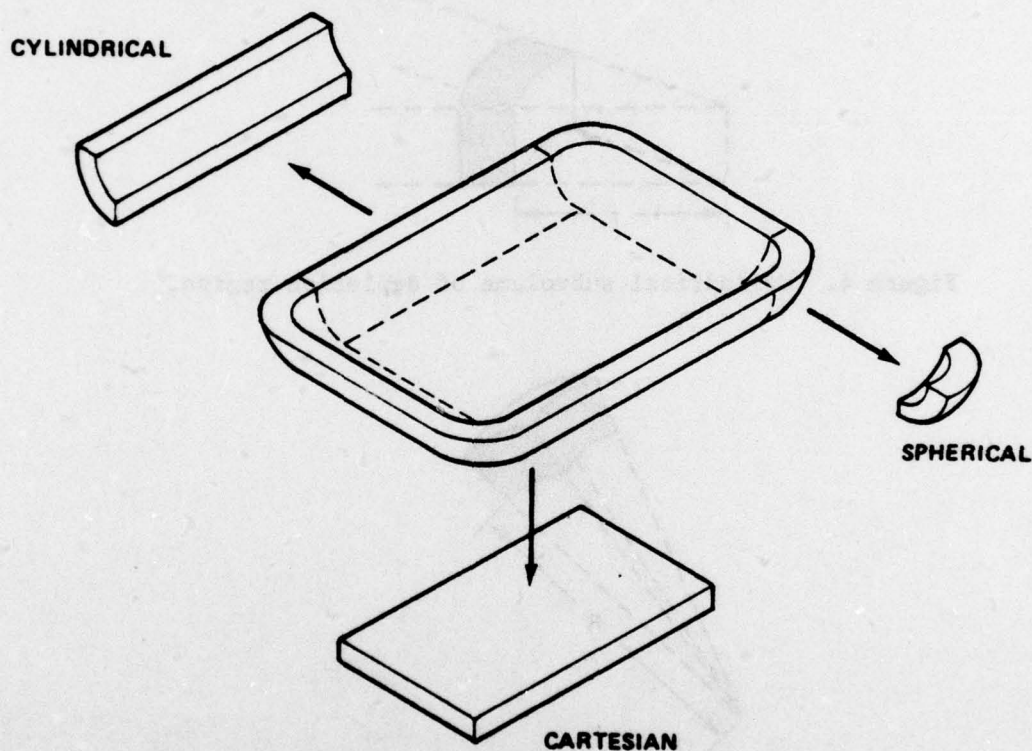


Figure 2. Division of idealized device into subregions.

The continuity equations for holes and electrons are

$$\frac{\partial p}{\partial t} = g_p - r_p - \frac{1}{q} \nabla \cdot \vec{J}_p \quad (1)$$

$$\frac{\partial n}{\partial t} = g_n - r_n + \frac{1}{q} \nabla \cdot \vec{J}_n \quad (2)$$



Figure 3. Cartesian subvolume of depletion region.

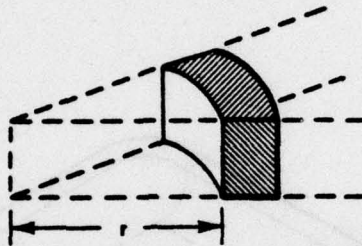


Figure 4. Cylindrical subvolume of depletion region.

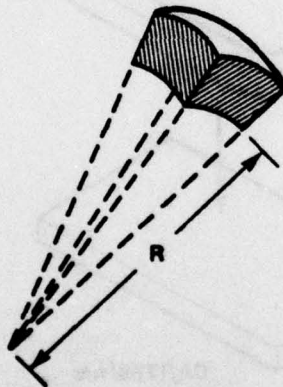


Figure 5. Spherical subvolume of depletion region.

For avalanche conditions, the generation rates may be assumed to be equal and to be much greater than the recombination rates:

$$g_p = g_n = g \quad (3)$$

$$r_p = r_n = 0 \quad . \quad (4)$$

For steady state conditions, Equations (1) and (2) then become

$$\nabla \cdot \vec{J}_p = qg \quad (5)$$

$$\nabla \cdot \vec{J}_n = -qg \quad . \quad (6)$$

The standard assumption for generation rate in bipolar semiconductor devices is that a two-carrier Townsend avalanche process takes place, so that the differential equation for hole (minority) current density in n-type material in cylindrical coordinates is found to be

$$\frac{1}{r} \frac{d}{dr} (r J_p) = -\alpha_n J_n - \alpha_p J_p \quad , \quad (7)$$

and the differential equation for electron (majority) current density under the same conditions is

$$\frac{1}{r} \frac{d}{dr} (r J_n) = \alpha_n J_n + \alpha_p J_p \quad . \quad (8)$$

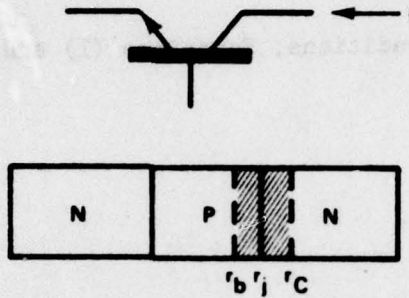
Integrating over the surface area,

$$\frac{dI_p}{dr} = -\alpha_n (I - I_p) - \alpha_p I_p$$

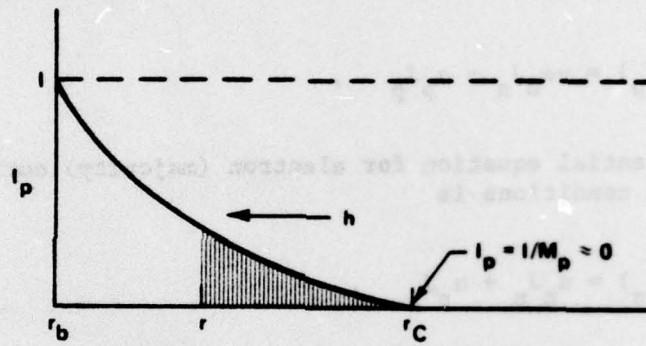
or, in standard form,

$$\frac{dI_p}{dr} - (\alpha_n - \alpha_p) I_p = -\alpha_n I \quad . \quad (9)$$

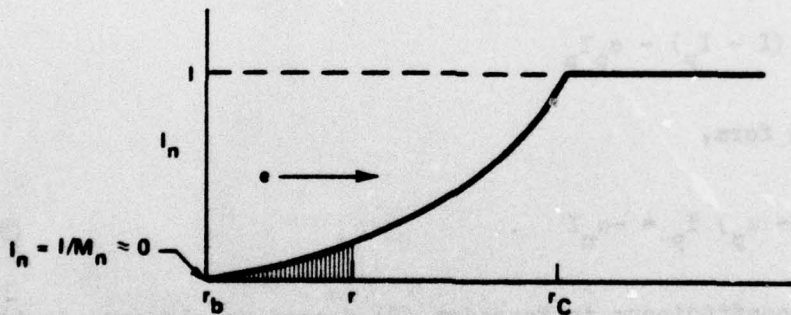
The ionization coefficients in Equation (9) depend on electric field intensity \mathcal{E} , which must be found by solving Poisson's equation. Under certain assumptions to be discussed later, the charge density term in Poisson's equation is essentially independent of currents I_p and I_n , so that Poisson's equation may be solved separately. As an example, the npn transistor of Figure 6 is considered. For "ordinary" avalanche breakdown in an npn transistor, the integral condition is:



(a) FRAME OF REFERENCE



(b) HOLE CURRENT



(c) ELECTRON CURRENT

Figure 6. Current through the collector-base junction of an npn transistor.

$$\lim_{M_p \rightarrow \infty} \left(1 - \frac{1}{M_p}\right) = 1 = \int_{r_b}^{r_o} \alpha_p e^{\int_r^{r_o} (\alpha_n - \alpha_p) dr'} dr \quad (10)$$

in which r_o is the value of r_c for which Equation (10) is balanced. It will be shown in the next section that under certain circumstances (corresponding to the sustaining voltage), breakdown can occur under very mild avalanche conditions, with only the requirement that [7]

$$\alpha_{f_{nnp}} M_n = 1 \quad (11)$$

Referring to Figure 6,

$$1 - \alpha_{f_{nnp}} = \int_{r_b}^{r_s} \alpha_n e^{-\int_{r_b}^r (\alpha_n - \alpha_p) dr'} dr \quad (12)$$

in which r_s is the value of r_c for which Equation (12) is balanced. Figure 7 is the pnp-equivalent of Figure 4. The differential equation for hole current is

$$\frac{dI_p}{dr} + (\alpha_n - \alpha_p) I_p = \alpha_n I \quad (13)$$

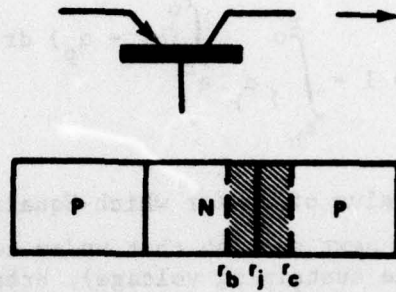
with boundary conditions

$$I_p(r_b) = \frac{I}{M_p} \quad (14)$$

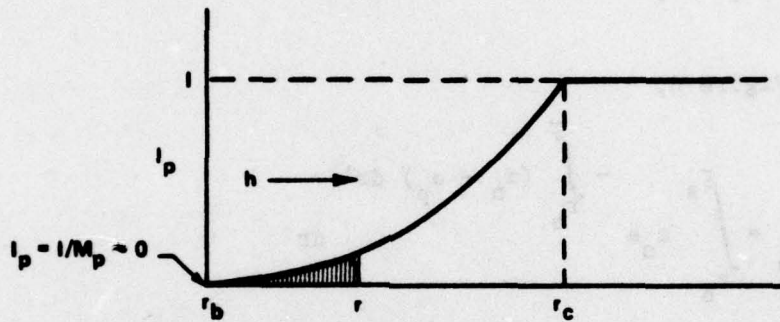
$$I_p(r_c) = I \quad (15)$$

and sustaining voltage condition

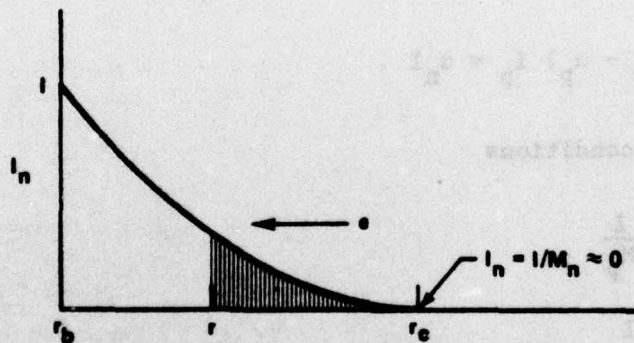
$$\alpha_{f_{pnp}} M_p = 1 \quad (16)$$



(a) FRAME OF REFERENCE



(b) HOLE CURRENT



(c) ELECTRON CURRENT

Figure 7. Current through the collector-base junction of a pnp transistor.

leading to the solutions

$$\lim_{M_p \rightarrow \infty} \left(1 - \frac{1}{M_p}\right) = 1 - \int_{r_b}^{r_0} \alpha_p e^{\int_{r_b}^r (\alpha_n - \alpha_p) dr'} dr \quad (17)$$

and

$$1 - \alpha_{f_{pnp}} = \int_{r_b}^{r_s} \alpha_p e^{\int_{r_b}^r (\alpha_n - \alpha_p) dr'} dr \quad (18)$$

Numerous approximations for the variation of ionization coefficients with electric field are available. The most common are [8]

$$\alpha = A_1 e^{a_1} \quad (19)$$

$$\alpha = A_2 e^{-a_2/\mathcal{E}} \quad (20)$$

$$\alpha = A_3 \exp(a_3/\mathcal{E}^2 + a_4/\mathcal{E} + a_5) \quad (21)$$

or combinations of these; the A and a constants are determined by curve fit. Table 1 shows typical values of A and a. Measured values are shown in Figure 8 [8,9].

TABLE 1. COEFFICIENTS FOR α CURVE FIT

	A_1	a_1	A_2	a_2
p	1.8×10^{-35}	7	2.25×10^7	3.26×10^6
n	1.8×10^{-35}	7	3.8×10^6	1.75×10^6
	A_3	a_3	a_4	a_5
p	2.22222×10^6	-1.64688×10^3	-8.22936×10^5	-0.3179
n	1.61290×10^6	-2.26641×10^3	-1.13297×10^6	-0.3188

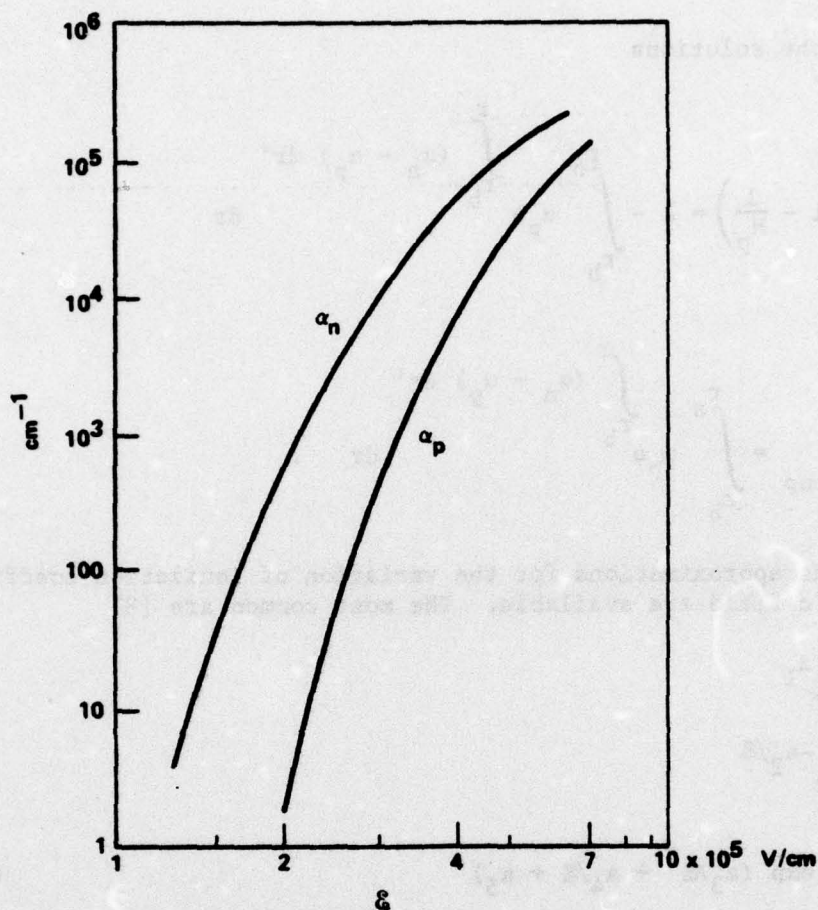


Figure 8. Measured ionization coefficients in silicon [8].

Equation (21) is said to yield a maximum of 2% error over the following ranges of E [8]:

$$2.33 \times 10^5 < E < 7.47 \times 10^5 \text{ V/cm for holes}$$

$$1.69 \times 10^5 < E < 5.42 \times 10^5 \text{ V/cm for electrons}$$

which compare quite favorably to the 10% to 20% accuracy quoted by the same reference for Equations (19) and (20). The data for Equation (21) in Reference 8, page 62, are reversed; those for Equation (20) are correct. Because α depends so strongly on E , the accuracy of the expression for α is very significant in calculations of avalanche breakdown voltage; this will be demonstrated.

Figure 9 shows avalanche breakdown voltage V_{br} versus doping density, calculated using the one-sided abrupt approximation and Equation (21), and Figure 10 shows the corresponding fields.

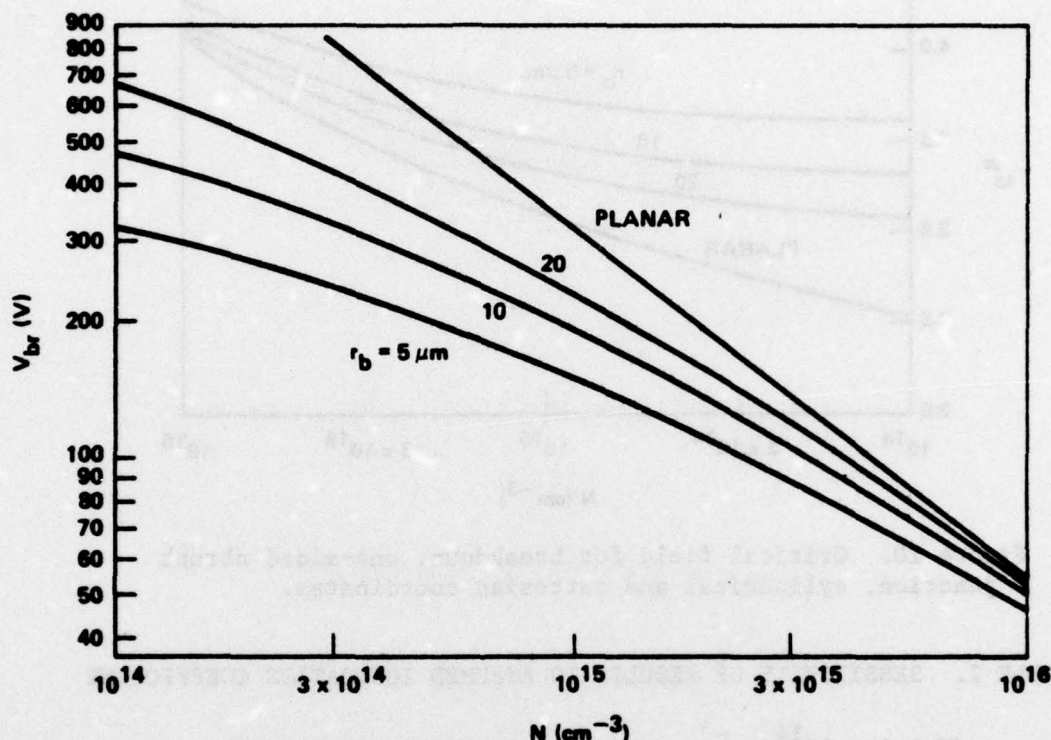


Figure 9. Junction breakdown, one-sided abrupt, cylindrical and cartesian (planar) coordinates.

Table 2 shows a comparison of results using Equations (19), (20), and (21) for a typical case. Figure 11 shows the corresponding $\alpha_n(r)$ and $\alpha_p(r)$ using Equations (20) and (21), respectively. The difference $\alpha_n - \alpha_p$ using Equation (21) has been included to demonstrate that α_p is almost negligible compared to α_n . The former cannot be neglected, however, because it is the term which leads to a finite width at breakdown. An interesting relation exists between the ionization coefficients in the range $265 \text{ kV/cm} \leq \mathcal{E} \leq 350 \text{ kV/cm}$ (most of the range of interest in avalanche breakdown), as indicated in Figure 12. The approximation (units of cm^{-1})

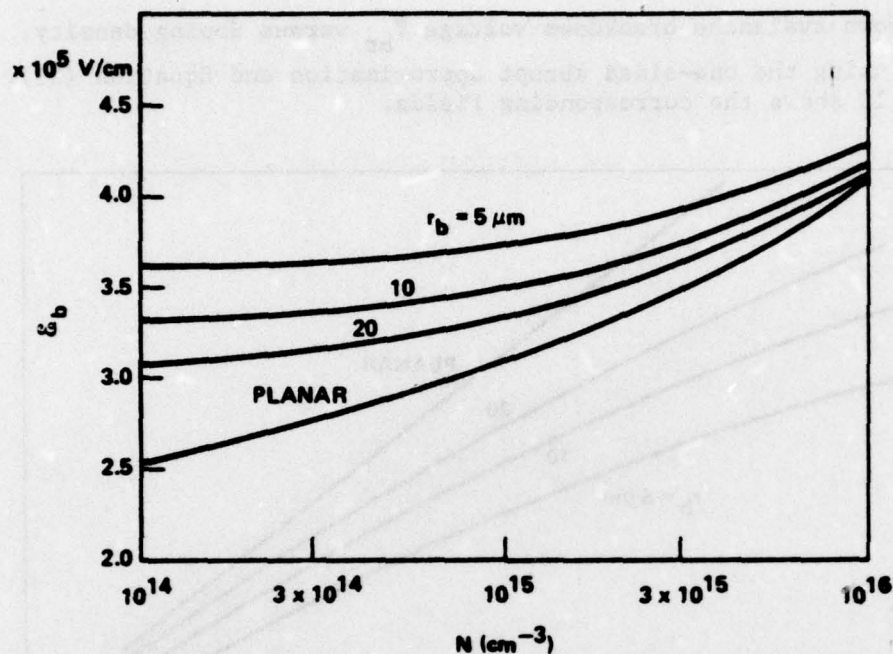


Figure 10. Critical field for breakdown, one-sided abrupt junction, cylindrical and cartesian coordinates.

TABLE 2. SENSITIVITY OF RESULTS TO ASSUMED IONIZATION COEFFICIENT

($N = 3 \times 10^{14} \text{ cm}^{-3}$, cylindrical, one-sided abrupt)

Equation	r_b (μm)	r_c (μm)	V_{br} (V)	ϵ (V/cm)
(62)	5	28.32	232.6	3.607×10^5
(63)	5	28.38	234.1	3.624×10^5
(64)	5	28.40	234.6	3.630×10^5

$$\alpha_n = 594 \sqrt{\alpha_p} \quad (22)$$

may be useful in analytical approximations for the breakdown voltage.

A "breakdown" condition (unlimited increase in collector current with no increase in base current) can occur in a common emitter circuit at collector-base junction voltages much below the avalanche voltage. Very little avalanching ($M \sim 1.02$) is required. To illustrate

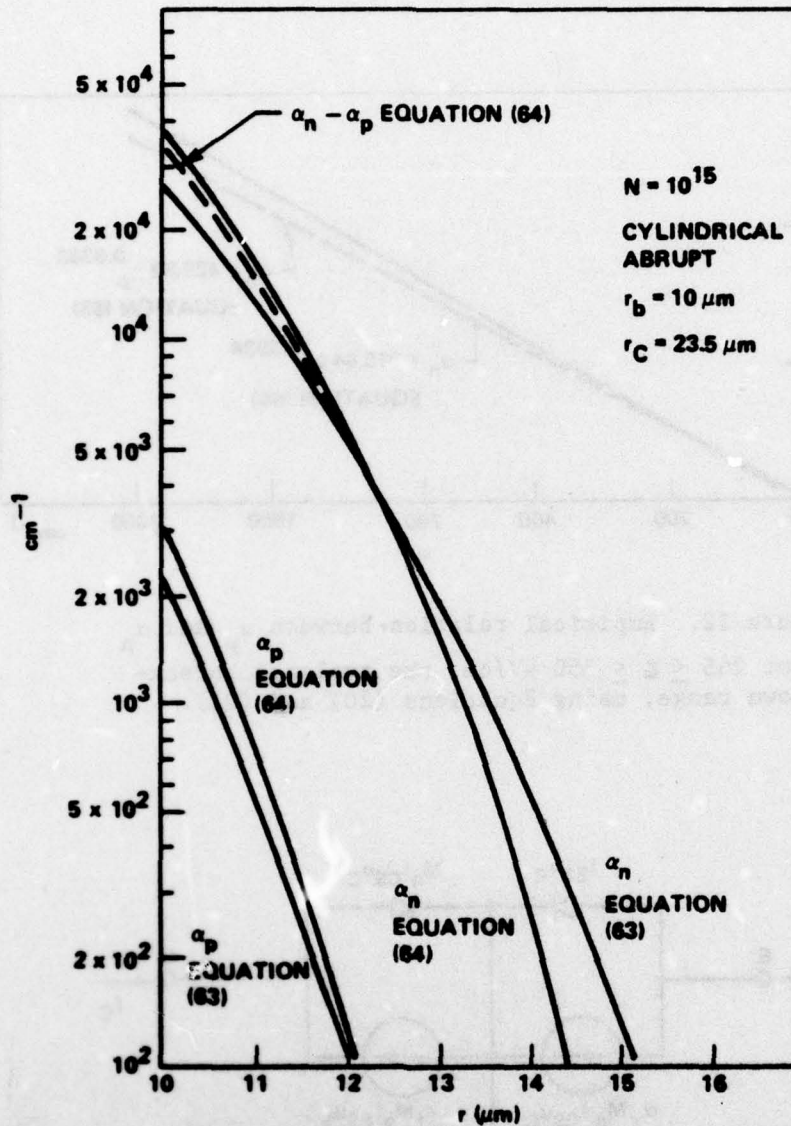


Figure 11. Ionization coefficients, using Equations (20) and (21).

this condition, an Ebers-Moll equivalent circuit of a pnp transistor with the collector-base junction in avalanche is given in Figure 13. The collector current under avalanche is given by

$$I_C = - \left[\frac{1 - \alpha_f \alpha_M}{1 - \alpha_f M_p} \right] M_n I_{CS} + \frac{\alpha_f M_p I_B}{1 - \alpha_f M_p} \quad (23)$$

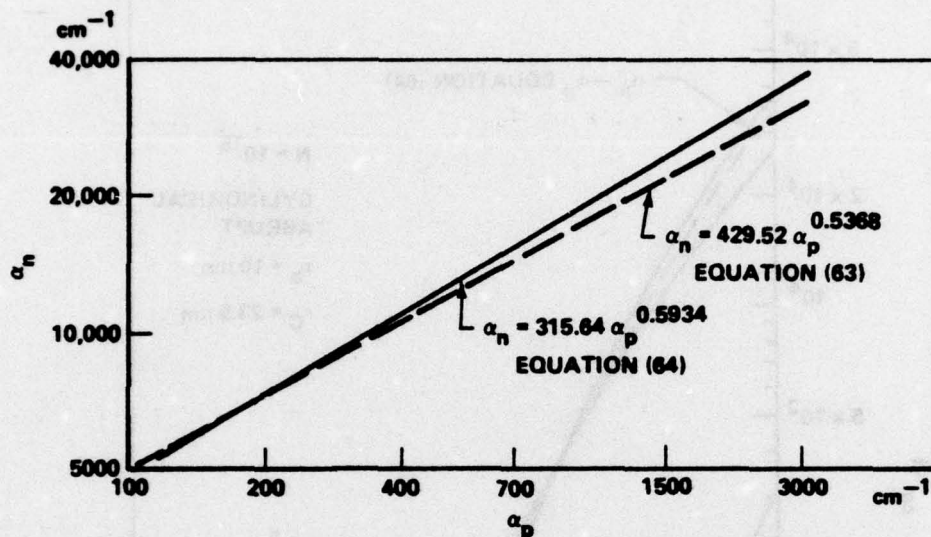


Figure 12. Empirical relation between α_p and α_n for $265 \leq E \leq 350$ kV/cm, the avalanche breakdown range, using Equations (20) and (21).

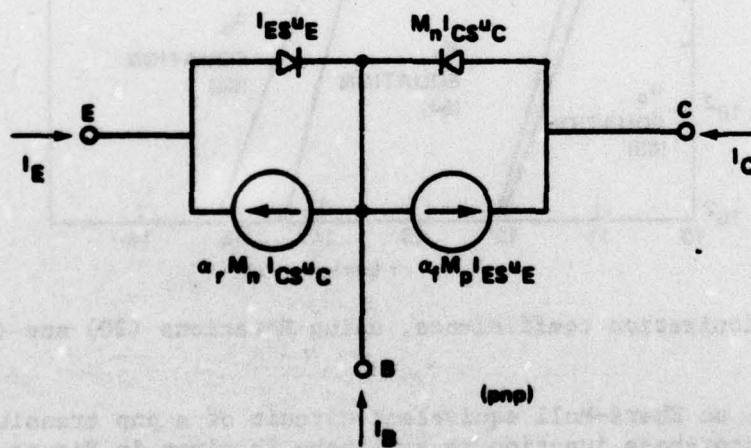


Figure 13. Ebers-Moll model for avalanche conditions.

The condition for unlimited increase in I_C is

$$\alpha_f M_p = 1 \quad , \quad (24)$$

i.e., such that the denominator of Equation (23) goes to zero.

The condition for $I_B = 0$, $I_E = -I_C$ is

$$I_C = - \left[\frac{1 - \alpha_f \alpha_r M_p}{1 - \alpha_f M_p} \right] M_n I_{CS} \quad . \quad (25)$$

The sustaining voltage V_s is defined as the voltage at which both conditions in Equation (24) and (25) are satisfied. The equation corresponding to Equation (24) for an npn transistor is

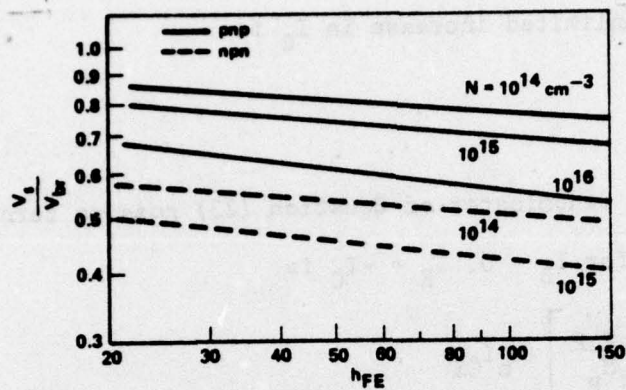
$$\alpha_f M_n = 1 \quad . \quad (26)$$

As noted previously,

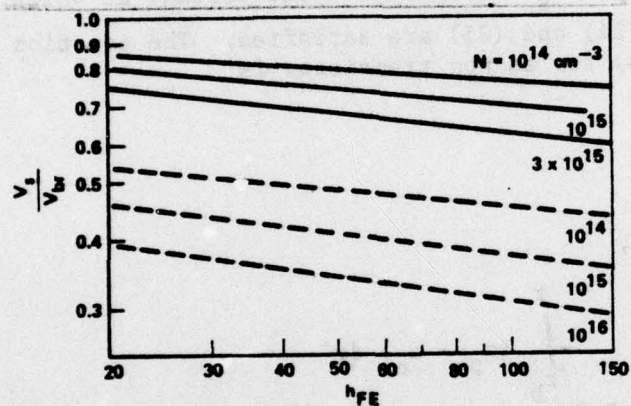
$$1 - \alpha_{f \text{ pnp}} = \int_{r_b}^{r_s} \alpha_p e^{-\int_{r_b}^r (\alpha_p - \alpha_n) dr'} dr \quad (27)$$

$$1 - \alpha_{f \text{ npn}} = \int_{r_b}^{r_s} \alpha_n e^{-\int_{r_b}^r (\alpha_p - \alpha_n) dr'} dr \quad (28)$$

in which r_s has been used as the value of r_c at the sustaining voltage to distinguish it from the value of r_c required for avalanche. Figure 14 shows V_s/V_{br} for the abrupt, one-sided junction approximation for the cylindrical, spherical, and cartesian geometries. Figure 15 shows the effect of a different doping profile for the cartesian case [4].



(a) CYLINDRICAL; BASE RADIUS = $20 \mu m$



(b) CARTESIAN (PLANAR)

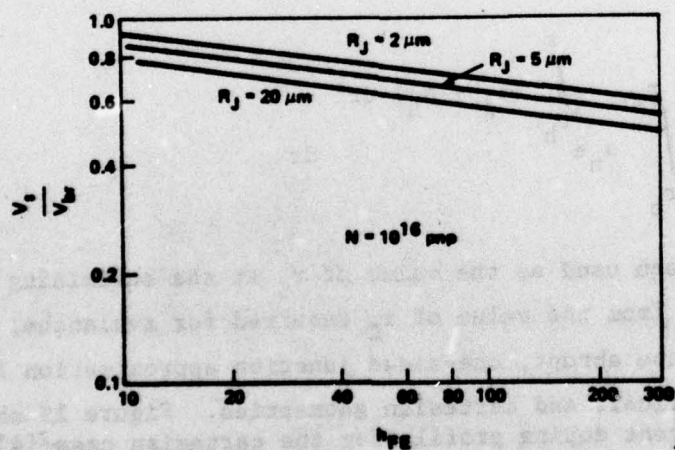


Figure 14. V_s/V_{br} for abrupt, one-sided junction approximation at collector.

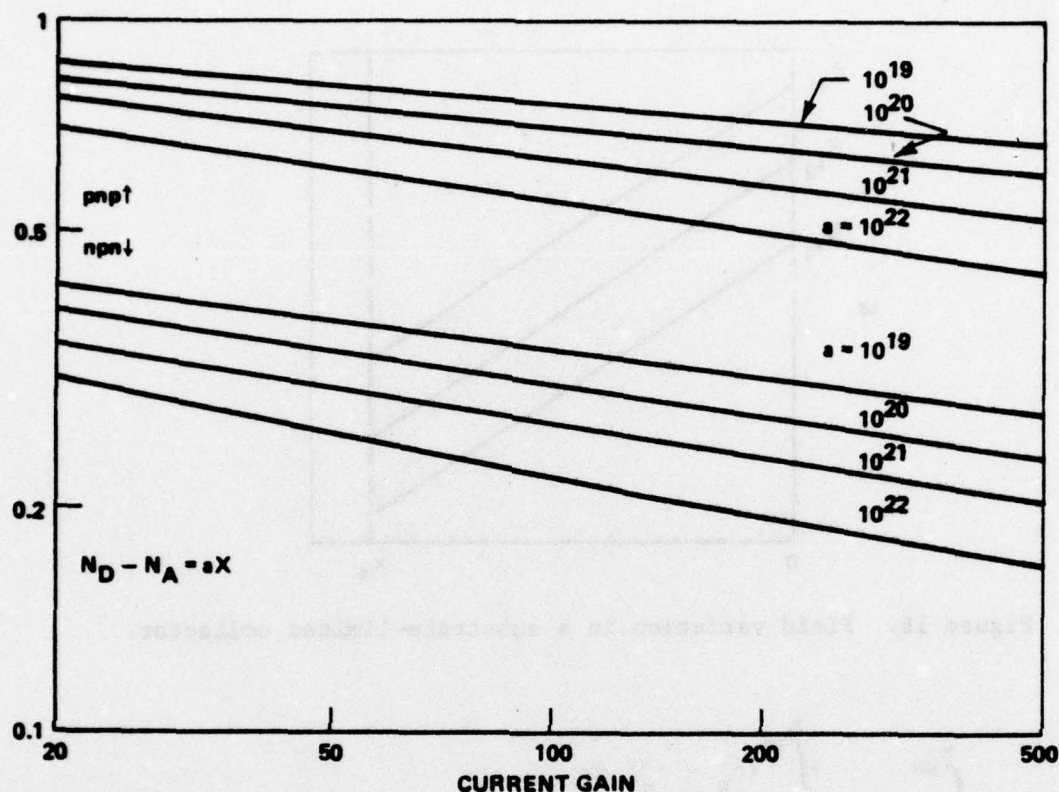


Figure 15. Normalized sustaining voltage versus current gain for linear graded junction transistors [4].

Reachthrough in epitaxial transistors is a special condition in which the collector-base junction depletion region becomes sufficiently wide that the entire lightly-doped collector bulk is depleted, the depletion layer edge reaches the heavily-doped substrate, and avalanche breakdown occurs at an abnormally low voltage. Expansion of the depletion region into the substrate is negligible, so a detailed analysis of the high-low junction effects at the substrate-collector bulk interface is not necessary. The assumption of negligible mobile carriers in solving Poisson's equation may still be made for fields between those required for reachthrough and avalanche, so that the electric field intensity may be calculated in the usual manner. Unlike the previous cases, the field intensity at x_{ss} (Figure 16) increases from zero with increasing voltage until avalanche breakdown is achieved. The field \mathcal{E}_b at the junction ($x = 0$) at avalanche due to reachthrough will be denoted \mathcal{E}_{rt} . The value of \mathcal{E}_{rt} is found by balancing the equation

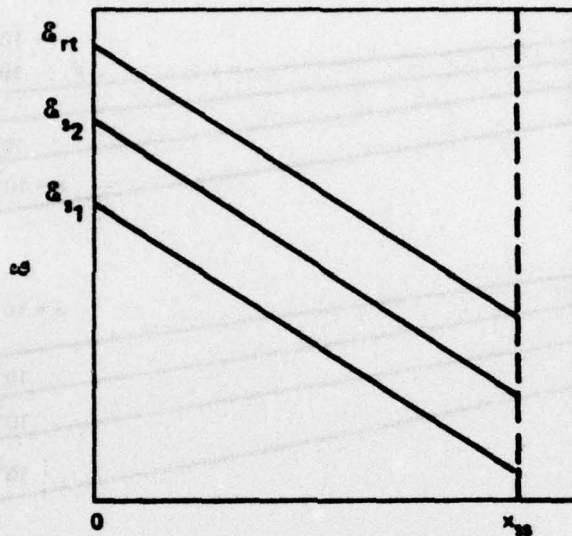


Figure 16. Field variation in a substrate-limited collector.

$$1 = \int_0^{x_{ss}} \alpha_n e^{-\int_x^{x_{ss}} (\alpha_n - \alpha_p) dx_1} dx \quad (29)$$

by an iterative process, with the upper limit fixed. Similarly, when $\phi(x_{ss}) > 0$,

$$1 - \alpha_{f_{pnp}} = \int_0^{x_{ss}} \alpha_p e^{\int_0^x (\alpha_n - \alpha_p) dx_1} dx \quad (30)$$

Because the upper limit is fixed, values of the field at the junction, ϕ_s , should be selected according to the equation

$$\phi_s = \frac{qN_A x_{ss}}{\epsilon} + \gamma \left(\phi_{rt} - \frac{qN_A x_{ss}}{\epsilon} \right) \quad (31)$$

in which values of γ are selected in the range $0 \leq \gamma \leq 1$ and a curve plotted. Figure 17 shows V_s/V_{br} for a typical case [4].

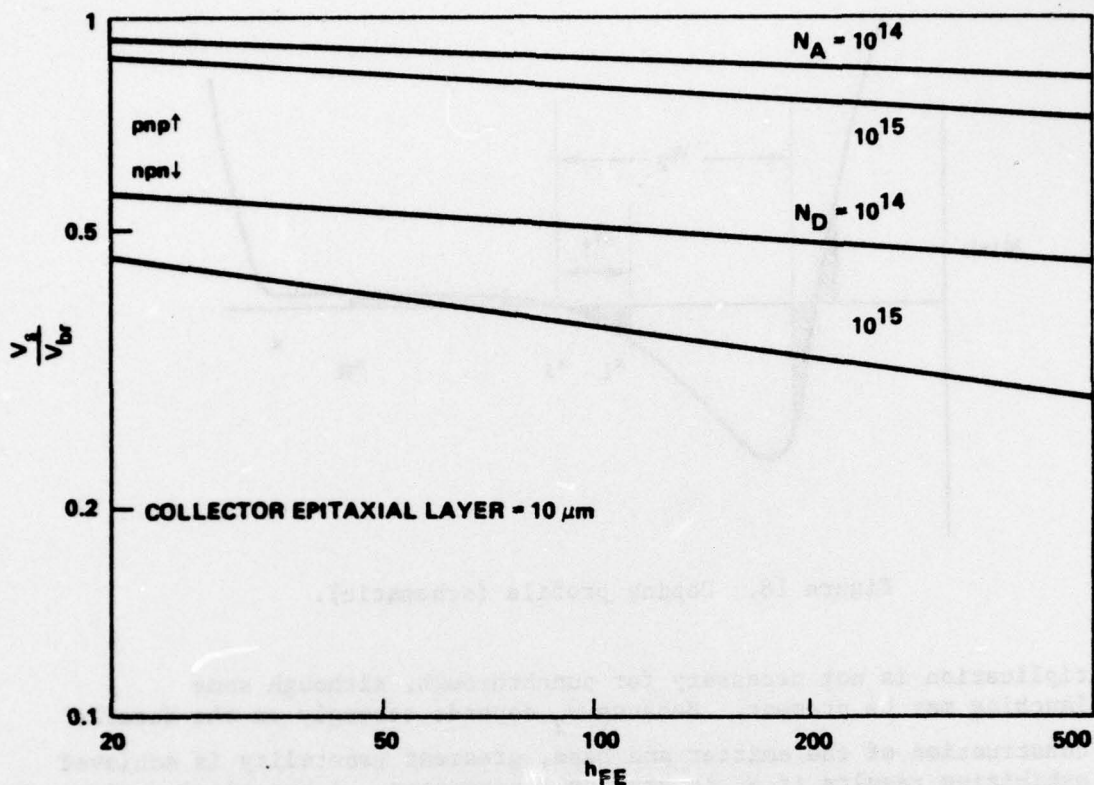


Figure 17. Normalized sustaining voltage versus current gain for epitaxial transistors with reachthrough [4].

Punchthrough is a linking up of the depletion layers of the emitter-base and collector-base junctions. In modern transistors, the base is more heavily doped than the collector, so the collector-base depletion layer extends farther into the collector than into the base for a given (reverse) bias on the collector-base junction. Emphasis on smaller, faster devices has led to very thin bases, thus increasing the likelihood of punchthrough and somewhat canceling this advantage of the heavily doped base. Because the emitter-base junction depletion layer is narrower at high emitter currents than it is at low emitter currents, worst-case operation is likely to be at high collector voltages and low currents. Neglecting any possible interaction effects when the two depletion layers come very close together, the condition for punchthrough is simply found by determining the width W_1 of the base side of the collector-base depletion layer (Figure 18) as a function of reverse bias voltage and comparing this width to the distance W_2 between the base edge of the emitter-base depletion layer and the collector-base junction. Punchthrough occurs when $W_1 = W_2$. Avalanche

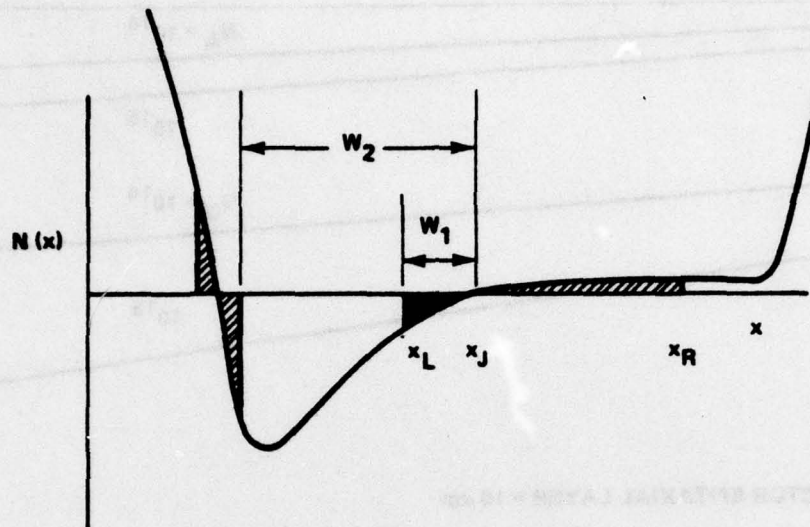


Figure 18. Doping profile (schematic).

multiplication is not necessary for punchthrough, although some avalanching may be present. Because W_2 depends strongly on the details of construction of the emitter and base, greatest generality is achieved in exhibiting results if W_2 is kept as a parameter. A practical design or analysis problem would then be, "Given an epitaxial double-diffused transistor with a punchthrough width W_2 , a collector-base junction sidewall radius r_j , and a collector epitaxial layer thickness d , which would occur first, avalanche (either sidewall or vertical), reachthrough, or punchthrough?" Fortunately, W_1 is already calculated as $x_L - x_J$ in finding the relationship between the width of the base side of the collector-base depletion layer and that of the collector side. Results of such a calculation are shown in Equation (21) and Figure 15 for a Gaussian diffusion into a constant epitaxial doping, roughly compatible with a Motorola 2N2222. Figure 19 shows reachthrough width versus collector-base bias voltage [8]. Phillips [10] points out that

$$V_{rt} = \frac{d}{x_0} \left(2 - \frac{d}{x_0} \right) V_{br} \quad (32)$$

in which x_0 is the width of the depletion region at ordinary breakdown. This can be rewritten

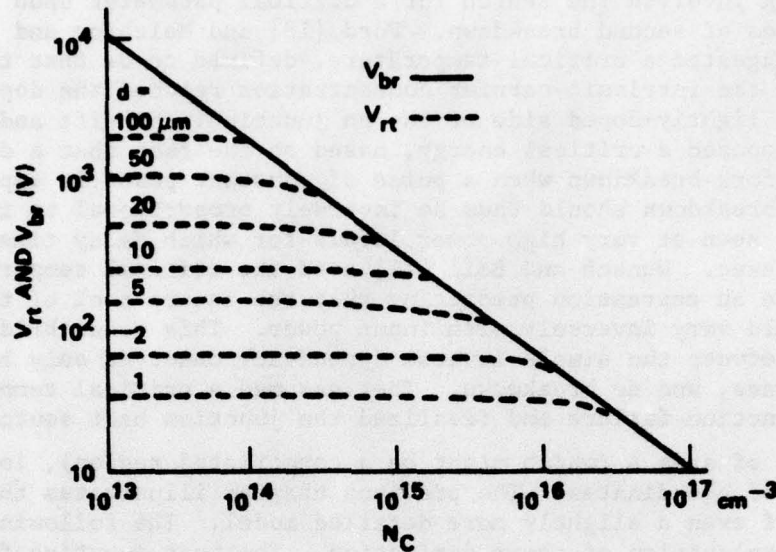


Figure 19. Avalanche and reachthrough voltages [8].

$$V_{rt} \approx d \sqrt{\frac{2qB_c V_{br}}{\epsilon}} - d^2 \left(\frac{qN_c}{2\epsilon} \right) \quad (33)$$

For a Motorola 2N2222, epitaxial doping density $N_c = 10^{15} \text{ cm}^{-3}$, and a typical value of d is $8 \text{ } \mu\text{m}$. Equation (33) predicts $V_{rt} = 202$, in good agreement with Figure 19. It should be noted that if $d = 8 \text{ } \mu\text{m}$, then $W_1 = 0.75 \text{ } \mu\text{m}$. Because the base width is nominally $1 \text{ } \mu\text{m}$, reachthrough will probably occur before punchthrough at normal forward bias.

III. SECOND BREAKDOWN

The literature on second breakdown is sufficiently voluminous that no attempt will be made to summarize more than a few key papers here. Budenstein [11] made a survey of papers published before 1970, Schafft and French [12] made a survey of very early work, and the IEEE Transactions on Electron Devices devoted two special issues to the subject [12,13]. These three references can be used as a source for nearly all of the early work on second breakdown. The most recent published work in the area at the time of this writing is probably that of Ward [14], Sutherland and Kennedy [15], and Raburn and Causey [16,17].

Early work involved the search for a critical parameter upon which to base analyses of second breakdown. Ford [18] and Melchior and Strutt [19] suggested a critical temperature, defined to be that temperature at which the intrinsic carrier concentration reached the doping density on the lightly-doped side of the pn junction. Schafft and French [20] proposed a critical energy, based on the fact that a delay time occurs before breakdown when a pulse of constant power is applied. Delay time to breakdown should thus be inversely proportional to input power; this is seen at very high power levels for which delay times are less than 100 nsec. Wunsch and Bell [21] used the critical temperature model to derive an expression predicting that the square root of the delay time would vary inversely with input power. This model bridges the time gap between the simple inverse dependency observed only below a few nanoseconds, and dc breakdown. They assumed a critical temperature T_f for junction failure and idealized the junction heat source as a plane source of area A (which might be a constricted region), located at the origin of coordinates. The previous chapter illustrates the complexities of even a slightly more detailed model. The following is a simplified explanation of their derivation. The heat equation for Joule heating and negligible thermal diffusion is

$$\rho_m c \frac{\partial T}{\partial t} = \vec{J} \cdot \vec{E} \quad (34)$$

in which ρ_m is the mass density and c is the heat capacity or specific heat per unit mass. Integrating over the volume,

$$\rho_m c F A = P \quad (35)$$

which defines a heat source F in terms of the dissipated power P and area A :

$$F = \frac{P}{c \rho_m A} \quad (36)$$

The source function for a plane source at the origin is

$$G = \frac{1}{\sqrt{4\pi at}} \quad (37)$$

so that, convolving F and G,

$$T_f - T_\infty = \int_0^{t_f} FG(t_f - t') dt' = \frac{P\sqrt{t_f}}{c \rho_m A \sqrt{\pi\alpha}} \quad (38)$$

in which t_f is the time between application of an electrical pulse and noticeable change in electrical characteristics; e.g., application of a large "rectangular" pulse of constant current leads to a roughly constant voltage until time t_f , when the voltage suddenly drops.

Rearranging Equation (38), the "Wunsch model" is found:

$$\frac{P}{A} = \frac{c \rho_m \sqrt{\pi\alpha} (T_f - T_\infty)}{\sqrt{t_f}} = \frac{\text{const}}{\sqrt{t_f}} \quad (39)$$

The model predicts the general trend in junction behavior over a large time regime, $10^{-8} \leq t_f \leq 10^{-2}$ sec for most devices, but (as noted by Wunsch and Bell) does not explain the large variation about the predicted value of P for any given t_f . The problem of sidewall avalanche breakdown versus vertical reachthrough discussed in Section II is one step in explaining this variation.

The critical energy model may be used to demonstrate the effects of short, high current pulses during which the heat generated has no time to leave the depletion layer. Whether current constricts during the rise time of the pulse or not at all is actually unknown. An idealized analysis will now be given which, like the Wunsch model, is very approximate but gives some insight into the effects of various parameters. It is assumed that the current constricts to a channel or channels of constant total area A_f (which will be some fraction of junction area A) and length L in a one-sided abrupt junction of doping density N. Because A_f will actually vary with time, the analysis will only be valid for pulses short enough that A_f does not vary significantly. The value of L can be approximated by the distance from metal contact to junction on the lightly doped side, or photographic data can be used. It is assumed all current flows through A_f . Then

$$J = \frac{I}{A_f} \quad (40)$$

and

$$g = g_o \frac{x}{L} = \frac{2V}{L^2} x \quad (41)$$

The heat generated per unit volume within the constriction(s) may be expressed as

$$\vec{J} \cdot \vec{g} = \frac{2 I V_J}{A_f L^2} x = \frac{2 P_J}{A_f L^2} x \quad (42)$$

The subscript J has been used on voltage and power to emphasize that these are values for the junction region, rather than external values. The heat equation, assuming an average value for K, may then be written

$$\frac{\partial T}{\partial t} = \alpha \frac{\partial^2 T}{\partial x^2} + \frac{2 P_J}{c \rho_m A_f L^2} \quad (43)$$

The boundary conditions which will be assumed are

$$T(x, 0) = T_\infty \quad (44)$$

$$T(0, t) = T_\infty \quad (45)$$

$$\frac{\partial T}{\partial x}(L, t) = 0 \quad (46)$$

Equation (45) is probably not too bad an assumption for the short pulses of interest. The last boundary condition [Equation (46)] is obtained by considering a symmetric abrupt junction for which the peak temperature is assumed for simplicity to occur at the metallurgical junction. A numerical solution to this problem can be found by using standard techniques; however, due to the approximations made, a simpler solution technique seems warranted. If a solution of the form

$$T = T_\infty + \sum_{i=1}^n a_i(t) x^i \quad (47)$$

is assumed using boundary conditions in Equations (14), (15) and (16) and $n = 2$, then

$$T_f = T(L, t_f) = T_\infty + \frac{P_J L}{c \rho_m A_f \alpha} \left(1 - e^{-2\alpha t_f / L^2} \right) . \quad (48)$$

For small t_f ,

$$\frac{P_J}{A} = \frac{c \rho_m L A_f (T_f - T_\infty)}{2 t_f A} = \frac{c \rho_m (T_f - T_\infty)}{t_f} \sqrt{\frac{V_J A_f}{2qN A}} . \quad (49)$$

Using $n = 3$,

$$T_f = T(L, t_f) = T_\infty + \frac{2P_J L}{3c \rho_m A_f \alpha} \left(1 - e^{-3\alpha t_f / L^2} \right) . \quad (50)$$

For small t_f , Equation (49) is again obtained. Equation (49) may also be obtained by using Laplace transforms. Solving Equations (44) through (46) leads to a complicated expression which may be simplified by the fact that the solution for small time t corresponds to large s in the transformed solution. This approximation again leads exactly to Equation (49). Equation (49) may be rewritten in terms of externally-measured values and V_{bulk} , the voltage drop across the ohmic bulk region, as

$$\frac{P}{A} = \frac{I V_{bulk}}{A} + \frac{c \rho_m (T_f - T_\infty)}{t_f} \sqrt{\frac{\epsilon(V_{appl} - V_{bulk})}{2qN}} \frac{A_f}{A} \quad (51)$$

in which P is the total power dissipated, and V_{appl} is the applied voltage (assumed constant). If V_{bulk} is negligible, a simple inverse relation exists between P and t_f . If not, an apparent "data spread" will occur. The same argument obviously applies to the Wunsch model. Some other points should be made about Equation (49). A single, constant T_f is assumed, as in the Wunsch model; only the qualitative success of the Wunsch model supports such an assumption. Experimental evidence exists for an inverse relationship between P_J and t_f , but experimental difficulties are encountered. Equation (51) predicts a dependence on doping density N . The effect of the square root is to lessen the data spread due to doping variations between samples.

A technique for direct observation of temperature variation in second breakdown was developed by Sunshine [22] and later used by Dumin [23]. This technique gave visual proof of the current constriction theory proposed by many authors [12,13]. Budenstein and his students [2,24] later refined this technique and made an extensive

study of current constriction or filamentation which forms the background for much of this report. The following is a brief description of some of Budenstein's work.

SOS diode test structures (Figure 20) can be made sufficiently thin that light can pass through both the silicon layer and the sapphire substrate. The light transmissivity at any point in the structure is proportional to the local temperature of the silicon. Using a lateral junction which is viewed edge-on (i.e., perpendicular to current flow) has a number of advantages: Current constrictions are easily observable (as darkened, high temperature areas), reachthrough problems of a vertical junction are avoided, and silicon-sapphire interface effects are less significant [25]. The limitation of the technique is that only the effects of self-heating are directly observable. Figures 21 and 22 show the optical arrangement used by Budenstein, et al. [2,24] to make temperature measurements. The probes shown in Figure 22 are used to pulse the device and to measure voltage and current. Figure 23 shows photographic results using this arrangement. Constant current pulses were used, and sufficient time was allowed to pass for development of well-defined hot spots (the dark spots on the photograph) at the junction. A large (reverse-bias) current pulse leads to the formation of many hot spots, while lower currents lead to fewer hot spots. The uniformity of spacing is the rule, rather than the exception. Nonuniformity is probably related to local inhomogeneity. As shown in Figure 24, the saturation (maximum) number of hot spots in the particular device used increased roughly linearly with the amplitude of the constant current pulse for currents greater than approximately 200 mA. If each hot spot is sufficiently isolated from the others that it can be treated independently and if a critical current density exists for onset of filamentation, then the experimentally observed uniformity of hot spot size [2,24] suggests that the number of hot spots should increase linearly with applied current. "If pulse duration is kept constant while progressively increasing pulse amplitude, the number of filaments increases to a saturation value. Further increase in pulse amplitude simply drives more current through existing filaments and ultimately leads to melt formation" [2]. Very large reverse bias pulsing leads to narrower filaments (elongated hot spots), and, as predicted by the model just discussed, more of them than at lower current levels. Forward bias pulsing leads to a single hot spot which is much wider (more diffuse) than those seen at reverse bias pulsing. The effective cross section of this hot spot is greater for current conduction and heat sinking than that of a single hot spot caused by reverse bias pulsing, so it is not surprising that damage occurs at higher currents and lower voltages than those required for damage at reverse bias. An extensive analysis of forward bias second breakdown has been performed by Navon [26].

In the reverse bias case, filament formation, or hot spot elongation, proceeds as illustrated schematically in Figure 25. The width changes very little as the length increases. The externally-measured

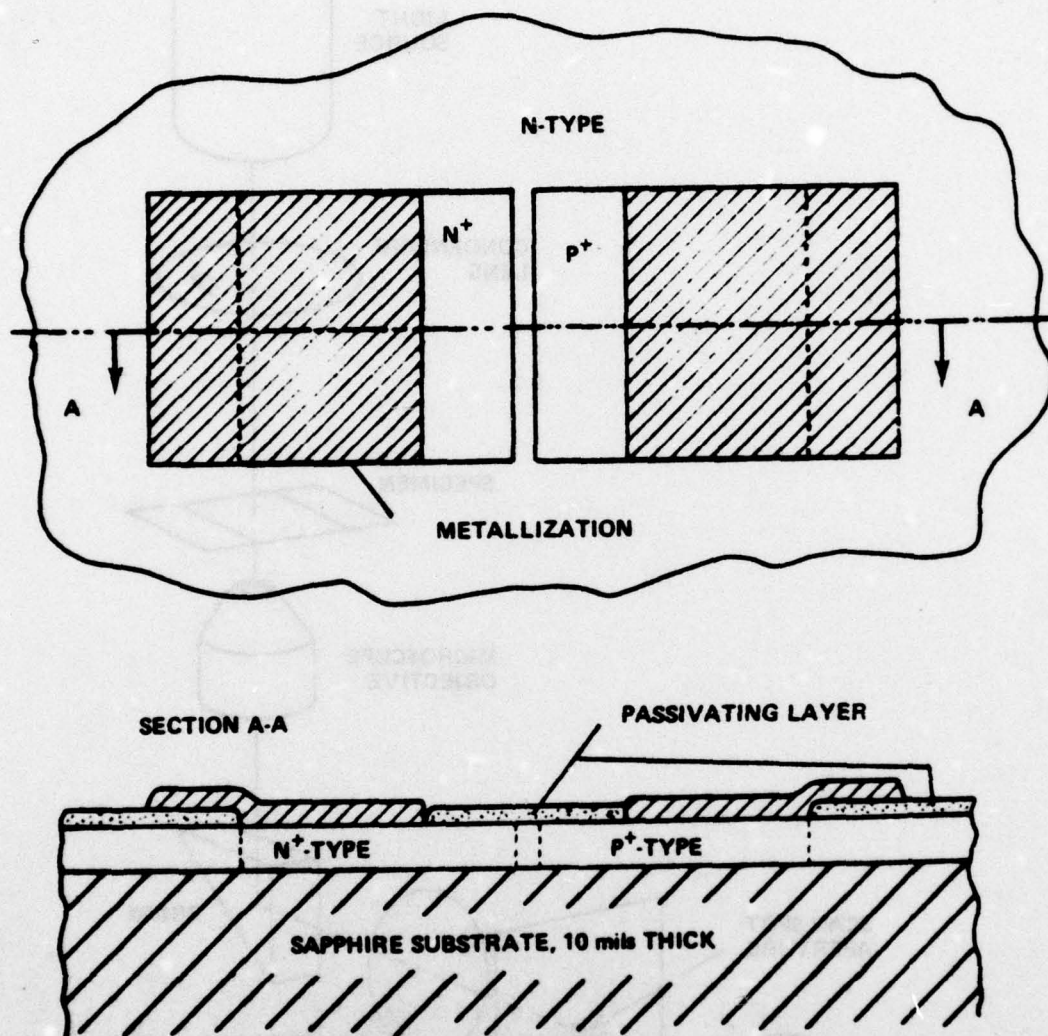


Figure 20. SOS diode geometry. Doping materials are diffused into an n-type silicon film to form p^+ and n^+ regions. Metallizations are of aluminum, and the passivating layers are thermally grown oxide [24].

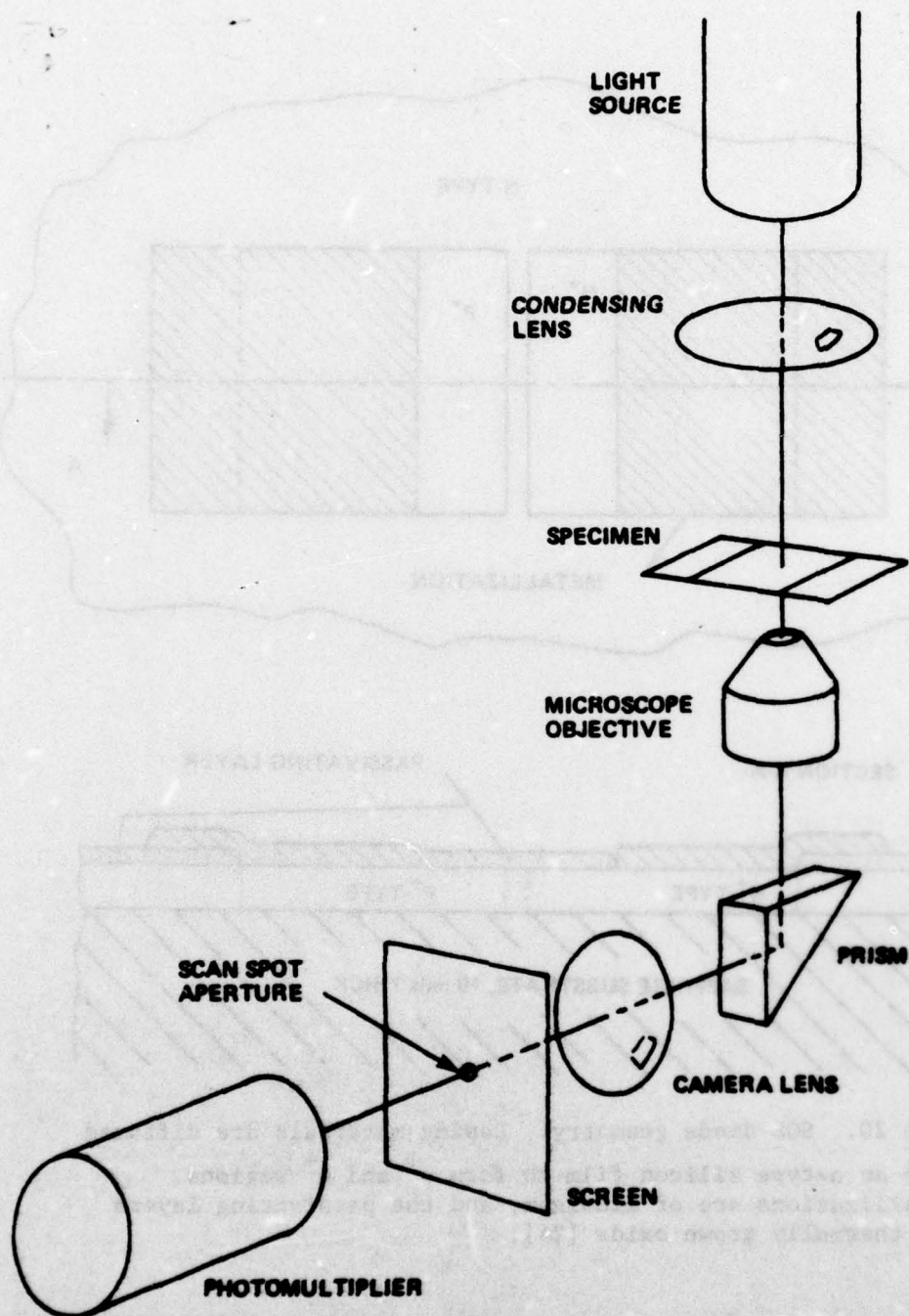


Figure 21. Optical arrangement used for making time-resolved temperature measurements [24].

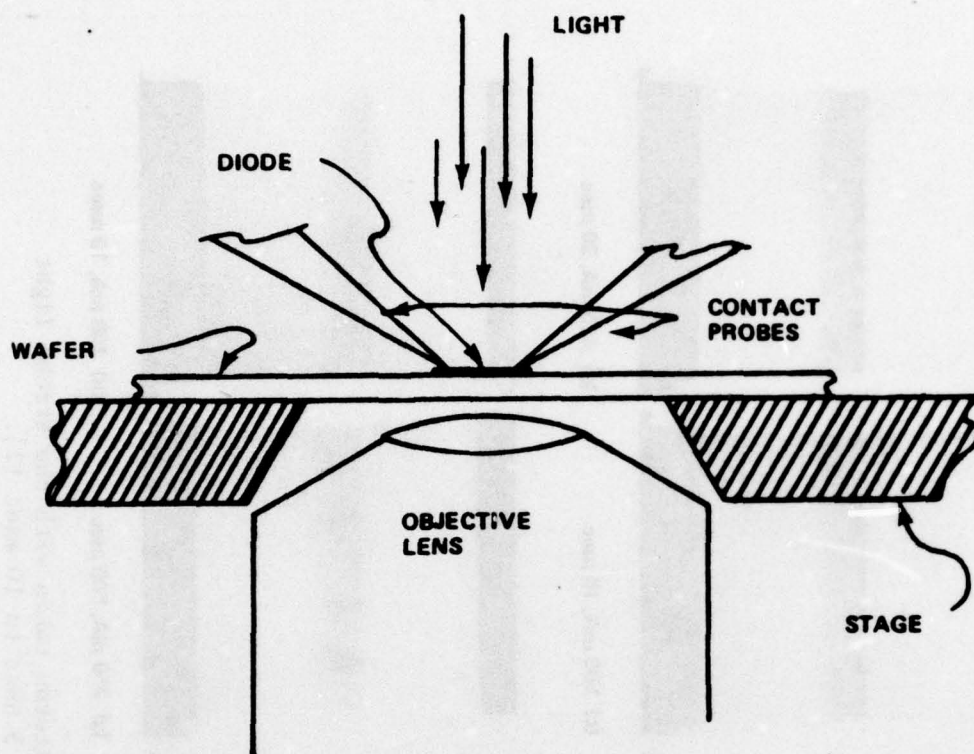


Figure 22. Experimental arrangement of the optical system used in making stroboscopic observations [24].

voltage should decrease more-or-less linearly with the elongation of the filament and may account for the gradual decrease in voltage seen in some voltage waveforms. When the filament reaches the other side of the high resistivity region, the "ballasting" effect of the high resistivity material is gone and essentially all of the voltage drop is across the filament, which is already so hot that the material in the filament is at or near the intrinsic temperature. A melt channel forms within the intrinsic channel almost immediately after the high resistivity region is bridged. An interesting indication of the temperature distribution around the hot spots is given schematically in Figure 26 which shows the decrease in avalanching next to the filament, due to lateral heat flow. A region of normal avalanche is seen in close proximity. The sapphire substrate acts as a heat sink not found in conventional diodes and transistors, so the latter are expected to have somewhat different thermal profiles than those shown in Figure 26. The filament on the right in Figure 26 is growing at the expense of the others; it will soon rob most of the current, stunting the growth rate of the other filaments and increasing its own. Figures 25 and 26 are based on observations made while watching a time-lapse color movie film of second breakdown in SOS diodes. The film was produced by

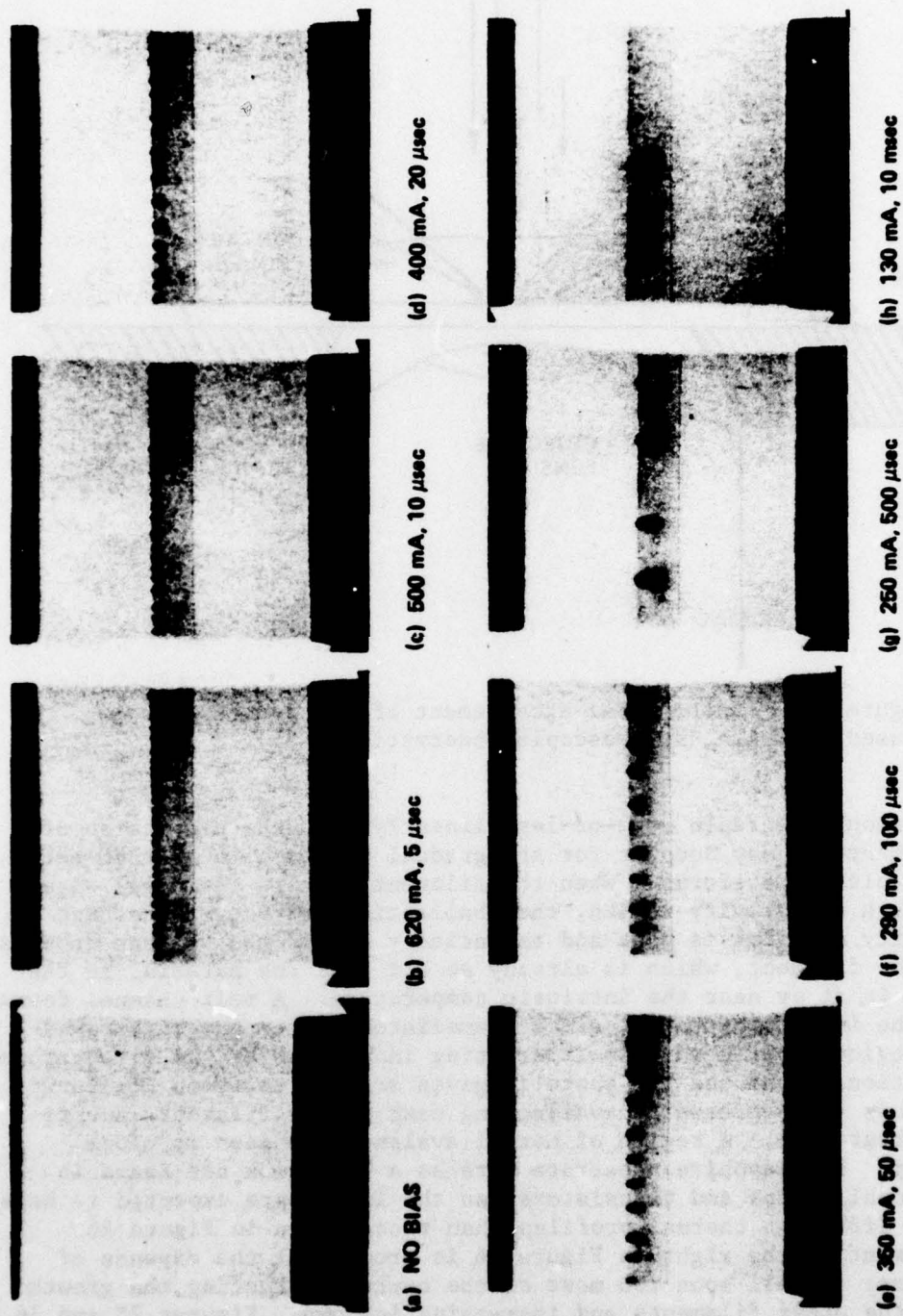


Figure 23. Optical transmission patterns taken with the strobe light for a range of pulse lengths from 5 μ sec to 10 msec [2].

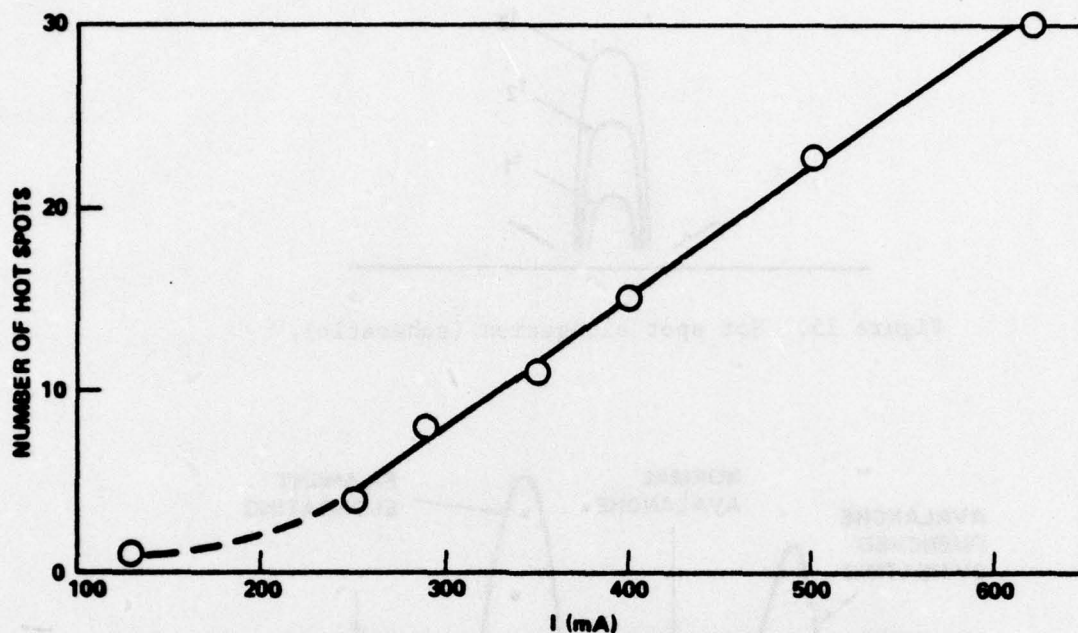


Figure 24. Saturation number of hot spots versus critical current for breakdown.

Budenstein, et al. [2] and has been shown at several technical meetings. Figure 27 shows a thermal mapping along a line (indicated by horizontal arrows) parallel to and at a separation of $12.7 \mu\text{m}$ from a junction in which the hot spots are clustered, rather than uniformly spaced [24]. Two very small, v-shaped metal protuberances (indicated by vertical arrows) along the edge of the upper metal pad seem to have a significant effect on the location of the hot spots. The protuberances and the surrounding high temperature darkened regions are far more evident on the original photograph. The protuberances were not seen initially and were observed to grow during the multiple pulsing required in setting up and taking data, possibly by electromigration of aluminum from the metal pad.* Because the location of the hot spots did not change over a long period of time (Each dot on the graph in Figure 27 represents a statistical average of hundreds of pulses, so that a week was required to obtain the data for this single graph.), it may be that nearly all of the electromigration took place very quickly. This would be consistent with a diffusion process. It should be mentioned that the averaging process is known to have lowered the "peaks" and filled in

*P. P. Budenstein, private communication, November 1976.

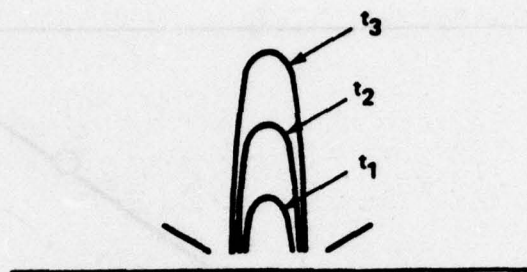


Figure 25. Hot spot elongation (schematic).

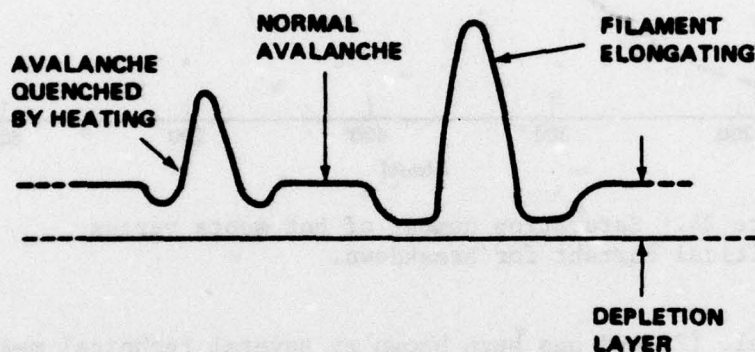


Figure 26. Temperature distribution along junction (schematic).

the "valleys" in the thermal map of Figure 27.* Such an effect of repeated pulsing is of more than academic interest; overvoltage transients are often in the form of damped sine waves, so the device could be hit several times in rapid succession.

The work of Berglund and Klein [27] serves to round out the information on combined thermal and electronic effects by providing a survey of thermal effects on switching of solids in general. It points out that the discharge of the junction capacitance must be considered in a thorough transient analysis of second breakdown. This discharge current is the displacement current term in the model used by Raburn and Causey [16].

*P. P. Budenstein, private communication, November 1976.

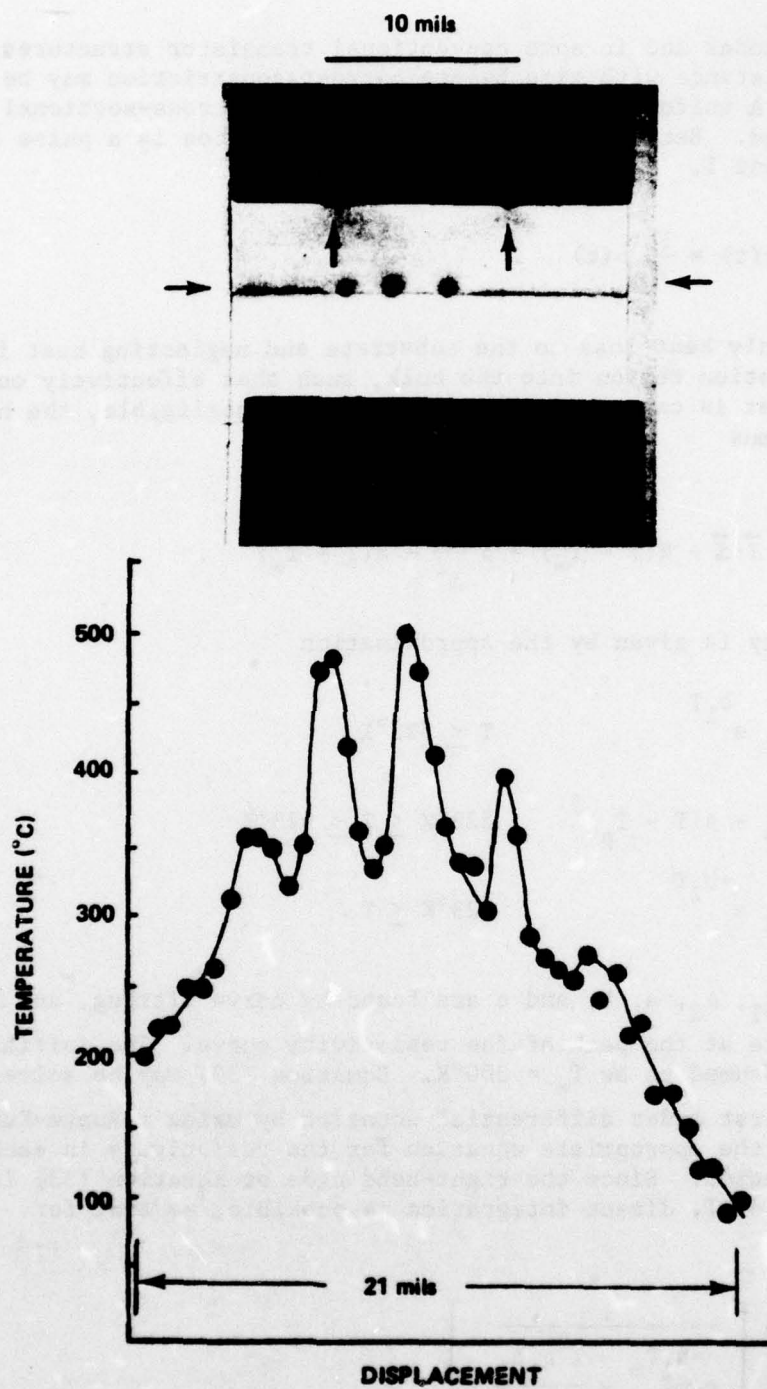


Figure 27. Time-resolved temperature measurement of the cross section of a diode exhibiting three junction channels [24].

In SOS diodes and in some conventional transistor structures, the change in resistance with time before current constriction may be significant. A uniformly conducting SOS diode of cross-sectional area A is considered. Because the standard test condition is a pulse of constant current I ,

$$V(t) = IR(t) = \frac{IL}{A} \rho(t) \quad . \quad (52)$$

Considering only heat loss to the substrate and neglecting heat flow from the depletion region into the bulk, such that effectively only a resistive sheet is considered and diffusion is negligible, the heat equation becomes

$$c\rho_m \frac{dT}{dt} = \vec{J} \cdot \vec{E} - H(T - T_\infty) = \rho \frac{I^2}{A} - H(T - T_\infty) \quad . \quad (53)$$

The resistivity is given by the approximation

$$\rho = \begin{cases} \rho_1 e^{b_1 T} & T \leq 523^\circ\text{K} \end{cases} \quad (54)$$

$$\rho = \begin{cases} \rho_0 - a(T - T_p)^2 & 523^\circ\text{K} \leq T \leq 623^\circ\text{K} \end{cases} \quad (55)$$

$$\rho = \begin{cases} \rho_2 e^{-b_2 T} & 623^\circ\text{K} \leq T \end{cases} \quad (56)$$

in which ρ_0 , ρ_1 , ρ_2 , a , b , and c are found by curve fitting, and T_p is the temperature at the peak of the resistivity curve. The initial temperature is assumed to be $T_\infty = 300^\circ\text{K}$. Equation (53) may be solved as a nonlinear first order differential equation by using a Runge-Kutta technique and the appropriate equation for the resistivity in each temperature regime. Since the right-hand side of Equation (53) is a function only of T , direct integration is possible, so that for $T \leq 523^\circ\text{K}$,

$$T = \frac{1}{b_1} \ln \left[\frac{1}{e^{-b_1 T_\infty} - \frac{I^2 \rho_1 b_1}{c_{\rho m} A^2} t} \right] \quad (57)$$

for $523^\circ\text{K} \leq T \leq 623^\circ\text{K}$,

$$\tau = \frac{\left(\sqrt{\frac{\rho_0}{a}} + \tau_p\right)\left(\sqrt{\frac{\rho_0}{a}} - \tau_p + \tau_1\right) - \left(\sqrt{\frac{\rho_0}{a}} - \tau_p\right)\left(\sqrt{\frac{\rho_0}{a}} + \tau_p - \tau_1\right) e^{-\frac{2\sqrt{\rho_0 a} \cdot I^2}{c\rho_m A^2} (t - \tau_1)}}{\sqrt{\frac{\rho_0}{a}} - \tau_p + \tau_1 + \left(\sqrt{\frac{\rho_0}{a}} + \tau_p - \tau_1\right) e^{-\frac{2\sqrt{\rho_0 a} \cdot I^2}{c\rho_m A^2} (t - \tau_1)}} \quad (58)$$

in which $T(t_1) = T_1 = 523^\circ\text{K}$, and for $623^\circ\text{K} \leq T$,

$$T = \frac{1}{b_2} \ln \left[e^{b_2 T_2} + \frac{I^2 \rho_2 b_2}{c\rho_m A^2} (t - t_2) \right] \quad (59)$$

in which $T(t_2) = T_2 = 623^\circ\text{K}$. The corresponding voltage in each case is found by calculating the resistivity and substituting it into Equation (52). For example, Equation (57) would be substituted into Equation (54), and Equation (54) would be substituted into Equation (52). Substituting some typical data [11], the effect of self-heating over the resistivity peak while still in uniform conduction is found to be as shown in Figures 28, 29, and 30. This may explain some of the perturbations seen on the voltage waveforms [11] prior to the sudden transition to a lower voltage state. Sutherland and Kennedy [15], Raburn and Causey [16], and Budenstein, et al. [2] have used a thermal equivalent circuit. Their results indicate that such an analysis is feasible if the source of the initial inhomogeneity can be found. As an example of such a thermal equivalent circuit, Figure 31 shows the Sutherland and Kennedy model [15]. W_p represents the power dissipation driving term in the heat equation, passive components R_x , R_T , and C_T represent terms arising from finite difference approximation to the partial derivatives, and T_{sink} represents the substrate temperature (assumed invariant, i.e., an ideal heat sink).

IV. MELT CHANNEL FORMATION AFTER SECOND BREAKDOWN

The conditions leading to second breakdown in a pn junction can be very difficult to analyze, even with a digital computer, but once current constriction or pinch-in has occurred, the analysis of actual damage can be greatly simplified. Budenstein, et al. [2], have shown by direct observation that damage due to second breakdown in a pn junction is the result of a melt channel forming within the intrinsic ("wash-out") pinch-in channel across the depletion region. Basically, melt channel formation is a moving-boundary problem with phase change

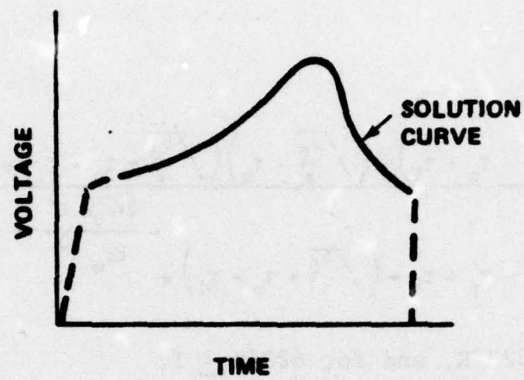


Figure 28. Nondestructive second breakdown due to resistivity variation, region of validity.

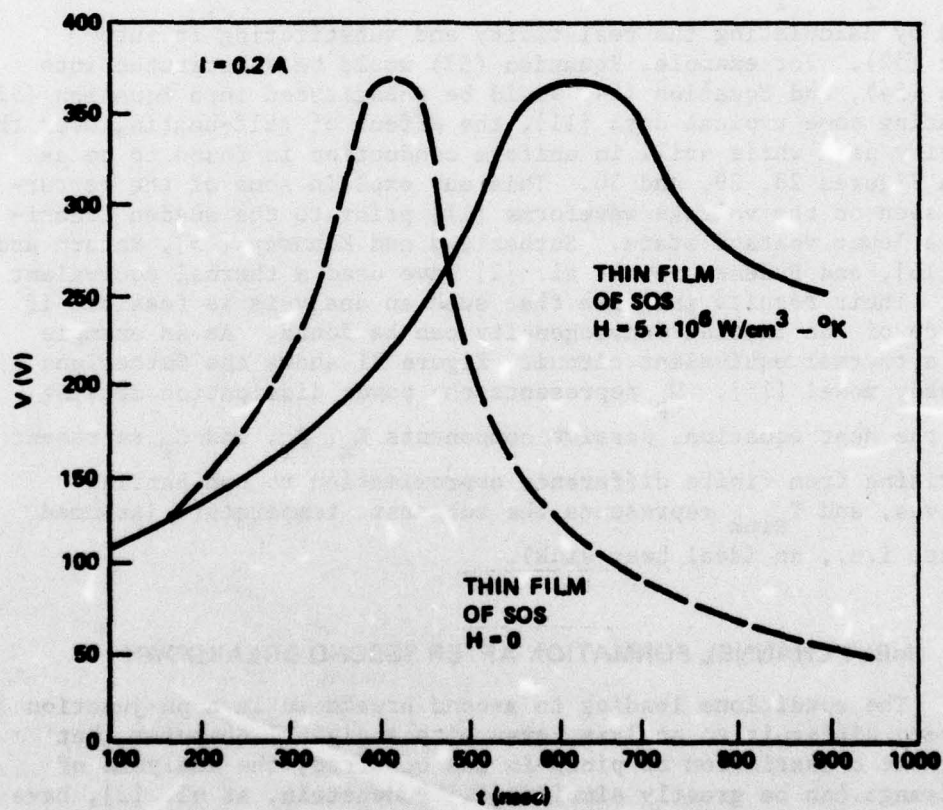


Figure 29. Nondestructive second breakdown due to resistivity variation, solution curve.

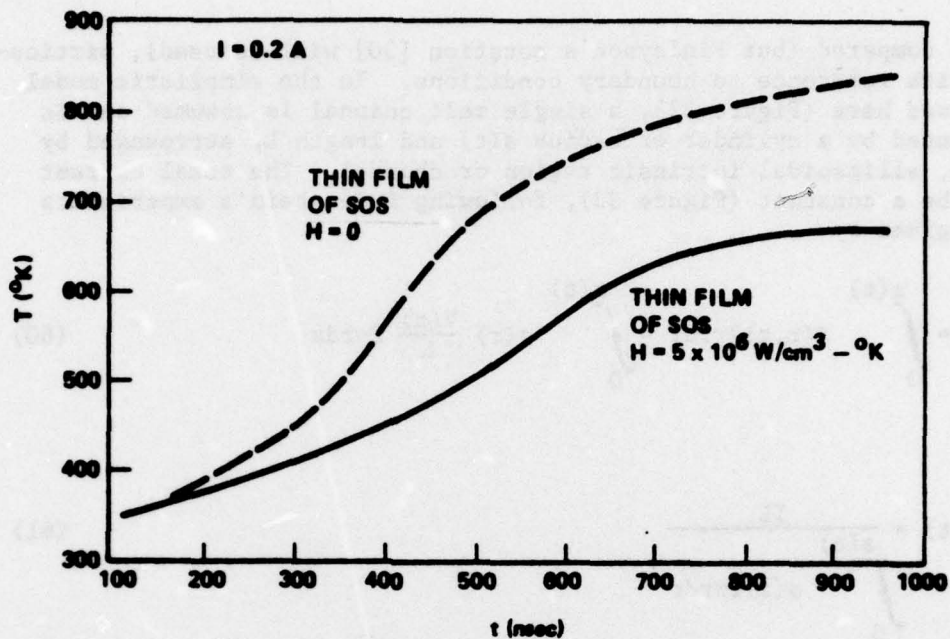


Figure 30. Temperature variation around resistivity peak.

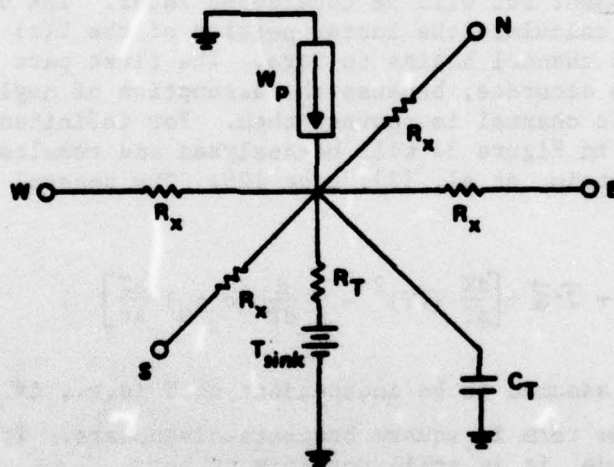


Figure 31. Sutherland and Kennedy model [15].

and cylindrical symmetry. Computer solutions for this problem under a variety of assumptions [2,25,28] have existed for some time, but an approximation technique of easy applicability has not. Moreover, some questions exist as to the assumptions made in these and other earlier analyses. The analysis of a related planar problem by Goodman [29]

will be compared (but Finlayson's notation [30] will be used), particularly with reference to boundary conditions. In the simplistic model to be used here (Figure 32), a single melt channel is assumed and is represented by a cylinder of radius $s(t)$ and length L , surrounded by a large, ellipsoidal intrinsic region or channel. The total current I will be a constant (Figure 33), following Budenstein's experiments and is given by

$$I = \int_0^{s(t)} J(r,t) 2\pi r dr = \int_0^{s(t)} \sigma(r) \frac{V(t)}{L} 2\pi r dr \quad (60)$$

or

$$V(t) = \frac{IL}{\int_0^{s(t)} \sigma(r) 2\pi r dr} \quad (61)$$

in which $J(r)$ is flowing in the z direction but varies in intensity with radial position. Current flow outside the melt channel will be neglected for the moment but will be considered later. The object of this analysis is to calculate the latter portion of the $V(t)$ curve, i.e., after the melt channel begins to form. The first part of the solution will not be accurate, because the assumption of negligible flow outside the melt channel is poorest then. For definiteness, the configuration shown in Figure 34 will be analyzed and results compared with those of Budenstein, et al. [2], page 128. The general equation is

$$c \rho_m \frac{\partial T}{\partial t} = KV^2T + \vec{J} \cdot \vec{E} + \left[\frac{dK}{dT} (VT)^2 - T \frac{d}{dT} (c \rho_m) \frac{\partial T}{\partial t} \right] \quad (62)$$

If K , c , and ρ_m are assumed to be independent of T (e.g., if average values are used), the term in square brackets disappears. If this assumption is not made, it is still possible to let

$$u = \frac{1}{K_m} \int_{T_m}^T KdT \quad (63)$$

in which T_m is the melting temperature of silicon, and K_m is the value of K just above the melting temperature. Then

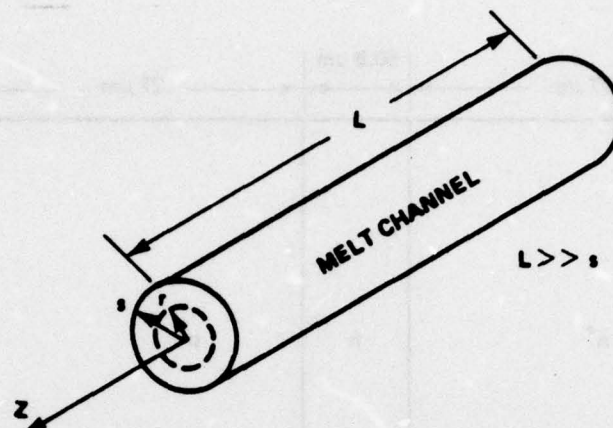


Figure 32. Idealized melt channel.

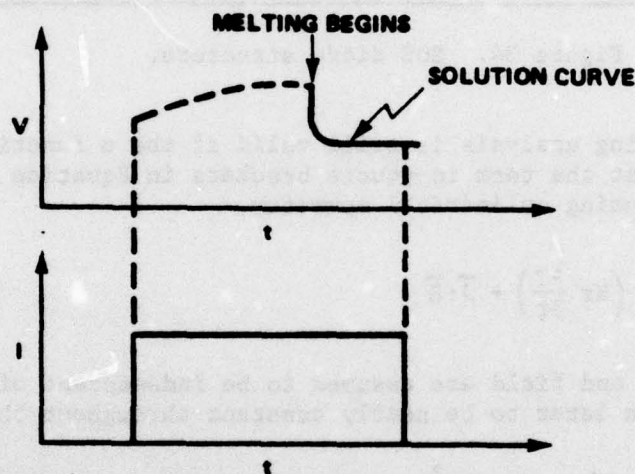


Figure 33. Real voltage and current waveforms [2].

$$\frac{\partial u}{\partial t} = K' \nabla^2 u + \frac{K'}{K_m} \vec{J} \cdot \vec{g} \quad (64)$$

where

$$K' = \frac{K}{c \rho_m + T \frac{d}{dT} (c \rho_m)} \quad (65)$$

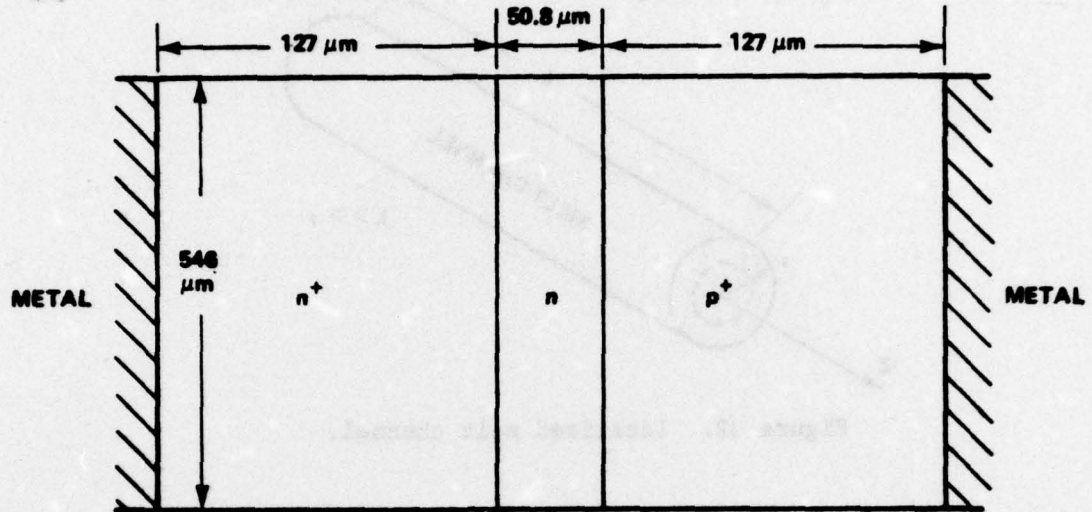


Figure 34. SOS diode structure.

Most of the following analysis is still valid if the u function is used. Assuming that the term in square brackets in Equation (62) disappears and assuming cylindrical symmetry,

$$\rho_m c \frac{\partial T}{\partial t} = \frac{1}{r} \frac{\partial}{\partial r} \left(K r \frac{\partial T}{\partial r} \right) + \vec{J} \cdot \vec{E} \quad (66)$$

or, if the current and field are assumed to be independent of r (temperature will be shown later to be nearly constant throughout the melt),

$$\rho_m c \frac{\partial T}{\partial t} = \frac{1}{r} \frac{\partial}{\partial r} \left(K r \frac{\partial T}{\partial r} \right) + \frac{\sigma V^2}{L^2} \quad (67)$$

in which σ is the electrical conductivity in $1/\text{ohm-m}$. The voltage $V(t)$ is the quantity ultimately sought and is found by solving first for the temperature $T(r,t)$. Boundary conditions are given by the Fourier equation and melting temperature at $r = s(t)$,

$$\rho_m \lambda \frac{ds}{dt} = - \left(K \frac{\partial T}{\partial r} \right) \Big|_{r=s_-} + \left(K \frac{\partial T}{\partial r} \right) \Big|_{r=s_+} \quad (68)$$

and

$$T(s,t) = T_m, \quad (69)$$

and the Fourier equation at $r = 0$

$$\left. \frac{\partial T}{\partial r} \right|_{r=0} = 0 \quad (70)$$

(which is required for a continuous second derivative). The symbol s_+ denotes the solid side of the melt-solid interface. Latent heat of melting λ in J/kg enters only at the boundary; the rest of the melt channel is above the melting temperature.

If a surface (e.g., the substrate or the top of the chip) loss term is included, Equation (67) can be written

$$c \rho_m \frac{\partial T}{\partial t} = \frac{1}{r} \frac{\partial}{\partial r} \left(r K \frac{\partial T}{\partial r} \right) - H (T - T_m) + g \quad (71)$$

Quantities σ , ρ_m , K , λ , and c are taken to be constants and equal to their estimated mean values over the temperature range of interest (Table 3). Where a range of temperatures is indicated, the numbers in parentheses were used for the calculations. Their approximation will be justified later. Then Equation (64) can be written

$$\frac{\partial T}{\partial t} = \frac{\alpha}{r} \frac{\partial}{\partial r} \left(r \frac{\partial T}{\partial r} \right) + g \quad (72)$$

and Equation (64) can be written

$$V = \frac{IL}{\pi s^2 \sigma} \quad (73)$$

in which

$$\alpha = \frac{K}{\rho_m c} \quad (74)$$

$$g = \frac{\sigma V^2}{c \rho_m L^2} = \frac{I^2}{c \rho_m \pi^2 s^4 \sigma} = \frac{I^2 \alpha}{\pi^2 \sigma K s^4} = \frac{\text{const}}{s^4} \quad (75)$$

For simplicity, the difference between K above and below the melting point is neglected.

TABLE 3. ESTIMATED THERMAL PROPERTIES OF MOLTEN SILICON

Symbol	Parameter	Measurement*
ρ_m	Mass Density	2490 kg/m ³
c	Heat Capacity per Unit Mass	917 to 1050 (982) J/kg-°K
λ	Latent Heat of Melting	9.17×10^5 to 1.8×10^6 (1.8×10^6) J/kg
K	Thermal Conductivity	22 W/m-°K
σ	Electrical Conductivity	10^6 1/ohm-m
α	Thermal Diffusivity	9×10^{-6} m ² /sec
T_m	Melting Temperature	1683 to 1696 (1683) °K
T_b	Boiling Temperature	2628 to 3418°K

*The user is urged to be cautious of these figures, which are taken from a variety of sources.

$$\left. \frac{dT}{dt} \right|_{r=s} = 0 = \left. \frac{\partial T}{\partial r} \right|_{r=s} \frac{ds}{dt} + \left. \frac{\partial T}{\partial t} \right|_{r=s} = \left. \frac{\partial T}{\partial r} \right|_{r=s} \frac{ds}{dt} + \frac{\alpha}{r} \frac{\partial}{\partial r} \left(r \frac{\partial T}{\partial r} \right) \Big|_{r=s} + g \quad (76)$$

Similarly, on the other side of the melt-solid interface,

$$\left. \frac{dT}{dt} \right|_{r=s_+} = 0 = \left. \frac{\partial T}{\partial r} \right|_{r=s_+} \frac{ds_+}{dt} + \frac{\alpha}{r} \frac{\partial}{\partial r} \left(r \frac{\partial T}{\partial r} \right) \Big|_{s_+} \quad (77)$$

The two expressions for the interface velocity must be equal:

$$\frac{ds}{dt} = \frac{ds_+}{dt} \quad (78)$$

Solutions to the heat equation must be found for each side of the interface. If an approximate solution of the form

$$T(r,t) = T_m - a(s-r) + b(s-r)^2 \quad (79)$$

is assumed for the melt side, then

$$\frac{ds}{dt} = -\frac{2\alpha}{s} - \frac{g}{a} \quad (80)$$

To find an expression for the temperature gradient outside the melt, it is necessary to solve

$$\frac{\partial T}{\partial t} = \frac{\alpha}{r} \frac{\partial}{\partial r} \left(r \frac{\partial T}{\partial r} \right) \quad (81)$$

subject to the conditions

$$T(r,0) = T_1 \quad (r > s) \quad (82)$$

$$T(\infty, t) = T_1 \quad (83)$$

$$T(s, t) = T_m \quad (84)$$

in which T_1 is the temperature at the edge of the hot spot. The hot spot is so large compared to the melt channel that, for the duration of a typical test pulse, it may be considered infinite in size and initially at constant temperature in the region around the melt. This is justified by the fact that the temperature peaks in Figure 25 are on the order of 50 μm in width, while the solution here is intended to be valid only until the melt diameter reaches approximately 1 μm . A more sophisticated approach to the SOS diode analysis would have to involve the assumption of an initial temperature distribution inside the hot spot (which would also have an outer moving boundary) and the generation of heat inside the intrinsic channel due to the small, but finite, current flowing there. For a conventional transistor, only the substrate loss term could be neglected. Continuing with the analysis,

$$T = T_1 + (T_m - T_1) \frac{E_1\left(\frac{r^2}{4\alpha t}\right)}{E_1\left(\frac{s^2}{4\alpha t}\right)} \quad (85)$$

in which $E_1(y) = -Ei(-y)$ is the integral

$$E_1(y) = \int_y^{\infty} \frac{e^{-t}}{t} dt \quad (86)$$

From Equation (77),

$$\frac{ds}{dt} = \frac{s}{2t} \quad (87)$$

The temperature ($r \leq s$) may then be written

$$T = T_m + \frac{gt(s^2 - r^2)}{s^2 + 4at} \quad (88)$$

Equation (85) may be used to find T for $r > s$, if desired. Equations 5.1.53 and 5.1.56 of Abramowitz and Stegun [31] may be used to evaluate the integral in Equation (86). The expression for $s(t)$ is found from either Equation (80) or Equation (87):

$$s = s_0 \sqrt{\frac{t}{t_0}} \equiv \delta \sqrt{t} \quad (89)$$

Equation (88) then becomes

$$T = T_m + \left[\frac{I^2 \alpha}{T_{\infty} K (\delta^2 + 4a)} \right] \frac{(s^2 - r^2)}{s^4} \quad (r \leq s) \quad (90)$$

and Equation (85) becomes

$$T = T_1 + (T_m - T_1) \frac{E_1\left(\frac{r^2 \delta^2}{4as^2}\right)}{E_1\left(\frac{Y^2}{4a}\right)} \quad (r \geq s) \quad (91)$$

For the data of interest here,

$$T = T_1 + (T_m - T_1) \frac{\left[2\ln\left(\frac{r\delta}{2as}\right) + \gamma - \left(\frac{r\delta}{2as}\right)^2 \right]}{\left[2\ln\left(\frac{\delta}{2\sqrt{a}}\right) + \gamma - \left(\frac{\delta}{2\sqrt{a}}\right)^2 \right]} \quad r \geq s \quad (92)$$

in which $\gamma = 0.57721\dots$ is Euler's constant. From Equation (67), the voltage is

$$V = \frac{IL}{\pi\sigma\delta t} \quad (93)$$

Figure 35 shows the melt channel radius versus time for an SOS diode. The physical model breaks down at very short times such that the resistance of the melt channel is comparable to the bulk resistance. As the melt channel diameter becomes comparable to the thickness of the silicon layer, its cross section will no longer be circular and the model is again inaccurate. Similar arguments hold for an ordinary diode or transistor junction. In a small transistor, the channel diameter could become comparable to the channel length, so that neglecting heat flow from the ends of the channel would no longer be valid. For the SOS diode shown previously in Figure 34, and $I = 0.56$ A, the temperature is essentially independent of position throughout the melt region. In other words, the second term in Equation (90) contributes almost nothing. The derivative of T with respect to r just inside the interface is not negligible and dominates the growth rate of $s(t)$. Figure 36 shows the temperature variation in and around the melt channel in an SOS diode. The particular SOS diode used for this example was relatively heavily doped, so that the partially-avalanching depletion region extended only a small portion of the way along the melt channel. The intrinsic channel was therefore surrounded by and in series with ohmic bulk material. The temperature profile corresponds to t_1 of Figure 37, which shows profiles for an epitaxial transistor, e.g., a 2N2222. Voltage variation with time depends strongly on resistance R_B of the material in parallel with the melt channel and will be considered later.

A very desirable improvement can be made by considering the current outside the melt channel to flow through a constant resistance R_B (this is a good approximation [2]; nearly all of this current will flow through the intrinsic channel. The heat generation by this external current can be shown to be negligible compared to that generated inside the melt. Then the melt channel and the rest of the junction share total current I (Figure 38) and

$$V(t) = \frac{I}{\frac{1}{R_B} + \frac{1}{L} \int_0^{s(t)} \sigma(r) 2\pi r dr} = \frac{I}{\frac{1}{R_B} + \frac{\sigma\pi s^2}{L}} \quad (94)$$

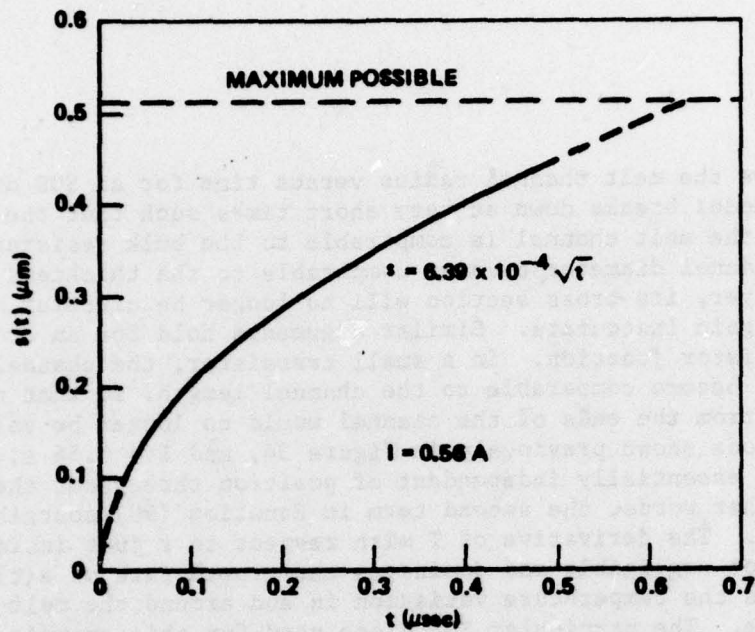


Figure 35. Radius of melt channel versus time.

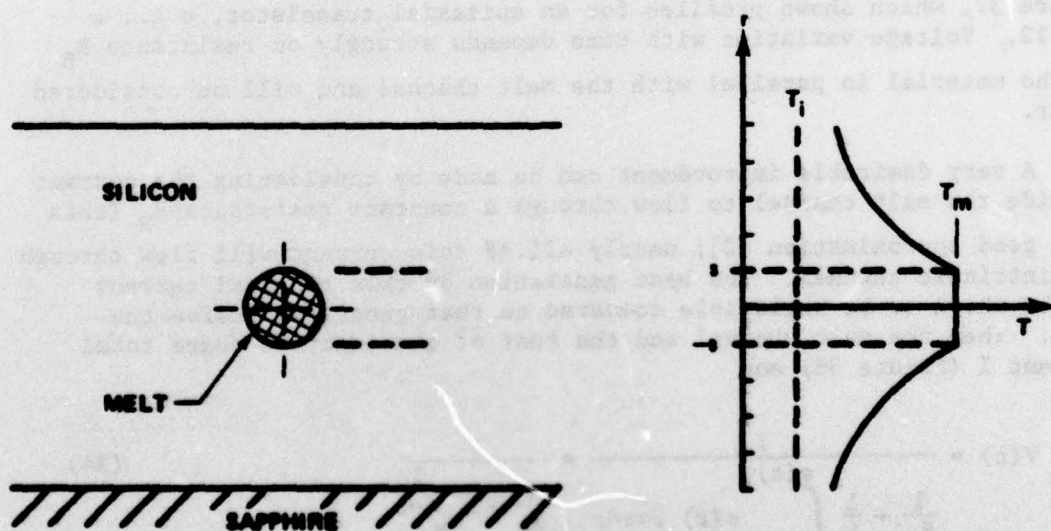


Figure 36. Temperature profile around melt, SOS diode.

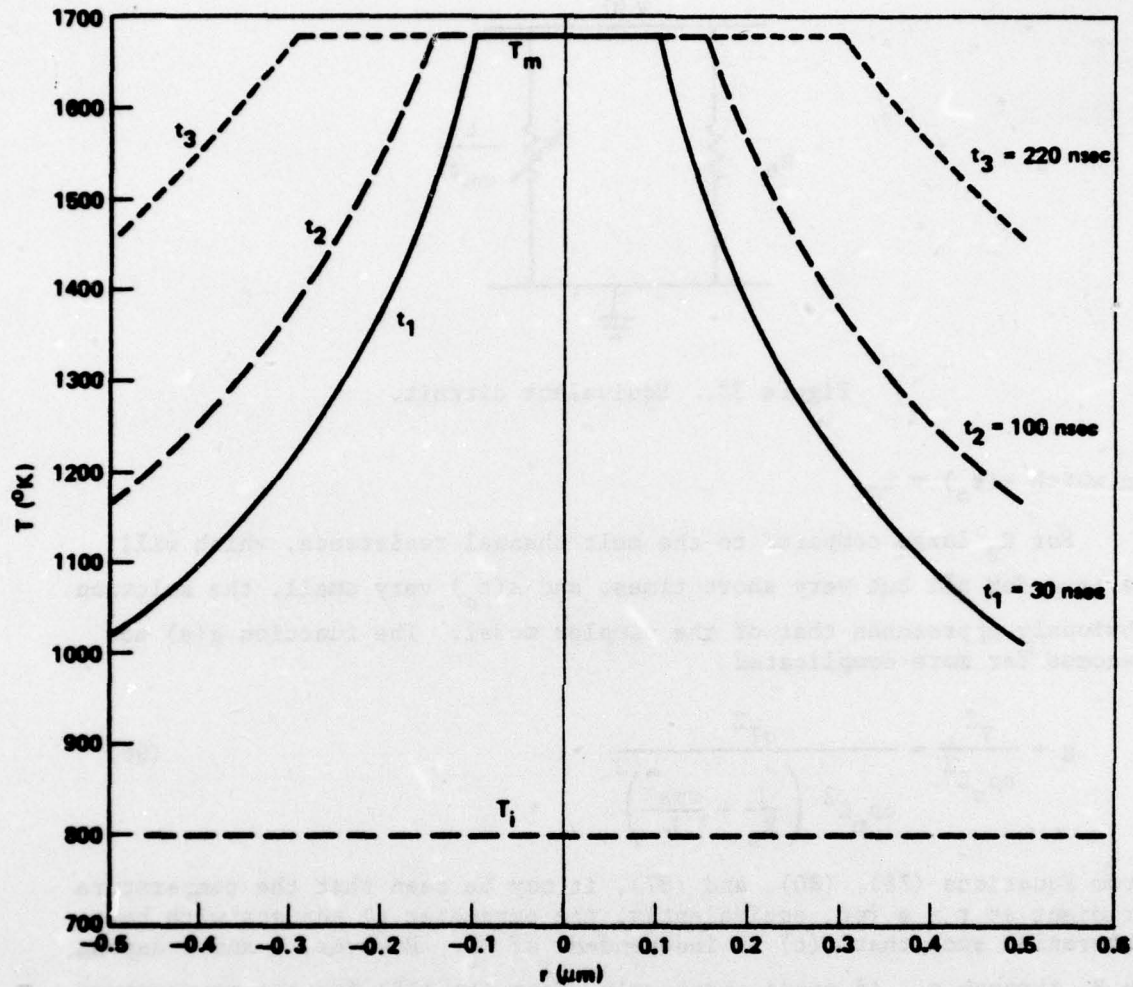


Figure 37. Temperature profile around melt, collector of epitaxial transistor.

in which R_B is the bulk resistance in parallel with the melt channel. The radius of the intrinsic channel increases with that of the melt channel, because the region around the melt channel becomes hotter as the melt channel grows. At $t = t_0$,

$$V_0 = V(t_0) = \frac{I}{\frac{1}{R_B} + \frac{\sigma \pi s_0^2}{L}} \quad (95)$$

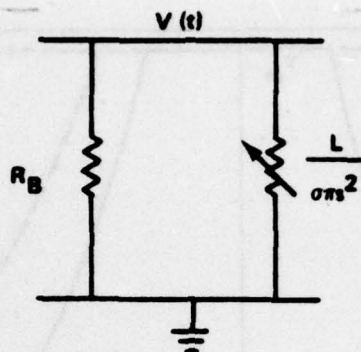


Figure 38. Equivalent circuit.

in which $s(t_0) = s_0$.

For R_B large compared to the melt channel resistance, which will be true for all but very short times, and $s(t_0)$ very small, the solution obviously approaches that of the simpler model. The function $g(s)$ now becomes far more complicated

$$g = \frac{V^2}{c\rho_m L^2} = \frac{\sigma I^2}{c\rho_m L^2 \left(\frac{1}{R_B} + \frac{\sigma \pi s^2}{L} \right)^2} \quad (96)$$

From Equations (78), (80), and (87), it may be seen that the temperature gradient at $r = s$ (or, equivalently, the parameter α) adjusts with heat generation such that $s(t)$ is independent of R_B . However, V and T depend on R_B through g . As noted previously, Equation (88) for the temperature in the melt is only significant in that it can be used to calculate the temperature gradient, which depends linearly on g . Using Equation (96), the temperature gradient at s for finite external resistance R_B is given by

$$\left. \frac{\partial T}{\partial r} \right|_{r=s} = - \frac{2sg}{\delta^2 + 4\alpha} = \frac{-2s\sigma I^2}{c\rho_m L^2 (\delta^2 + 4\alpha) \left(\frac{1}{R_B} + \frac{\sigma \pi s^2}{L} \right)^2} \quad (97)$$

By differentiating Equation (91) with respect to r and using Equations (68) and (97), the percentage of heat leaving the melt without contributing to further melting may be found. The heat which does not contribute to melting increases as s^2/I^2 . For the SOS diodes used by

Budenstein, et al. [2], at $I = 0.56$ A, this amounts to approximately 20% of the outflow when the melt channel diameter becomes comparable to the silicon thickness. For very short times, the heat leaving the melt channel may be assumed to go entirely into melting more silicon. This simplifies the analysis considerably, when valid, and corresponds to Goodman's approximation [29]. The general utility of Goodman's approximation for melt channel analysis is limited to very short times, corresponding to those at which the physical model is least accurate and to very long times when the channel is no longer cylindrical.

As illustrated in Figure 39, the voltage rises slightly during the pulse due to self-heating. The peak value may be taken equal to IR_B , yielding R_B immediately. If L is known from photomicrographs or electrical measurements, then a V_0 can arbitrarily be selected just below the knee of the curve in Figure 39 and the corresponding s_0 can be found from Equation (95). Substituting Equation (89) into Equation (94),

$$V = \frac{IR_B}{1 + \frac{\sigma\pi\delta^2 R_B}{L} t} \quad (98)$$

The value of δ can be found by curve fitting. As shown in Figure 40, the solution is valid for the falling portion of the curve until the melt channel diameter becomes comparable to the thickness of the silicon layer.

Qualitative agreement with experimental data by Budenstein, et al. [2] after the first few nanoseconds is fairly good. While linear approximations could have been used for λ , σ , K , etc. instead of their estimated mean values, the additional complication did not seem warranted in view of the approximations inherent in the model itself, the extreme lack of good data on the thermal properties of molten silicon, and the qualitative agreement with the experiment. As pointed out by Goodman [29], some improvement is possible if a cubic solution is assumed instead of the quadratic solution of Equation (78). If n channels are present, the total current I may be divided by n and used in the analysis just presented, provided that the separation between channels is large enough that the external temperature distributions given by Equation (91) have negligible overlap.

Budenstein's SOS devices are sufficiently thin that the cylindrical melt channel quickly reaches both the surface and the interface with the sapphire, becoming ribbon-like rather than cylindrical in less than a microsecond. In the following analysis, the growth of this ribbon of molten silicon will be considered. The problems of large channels

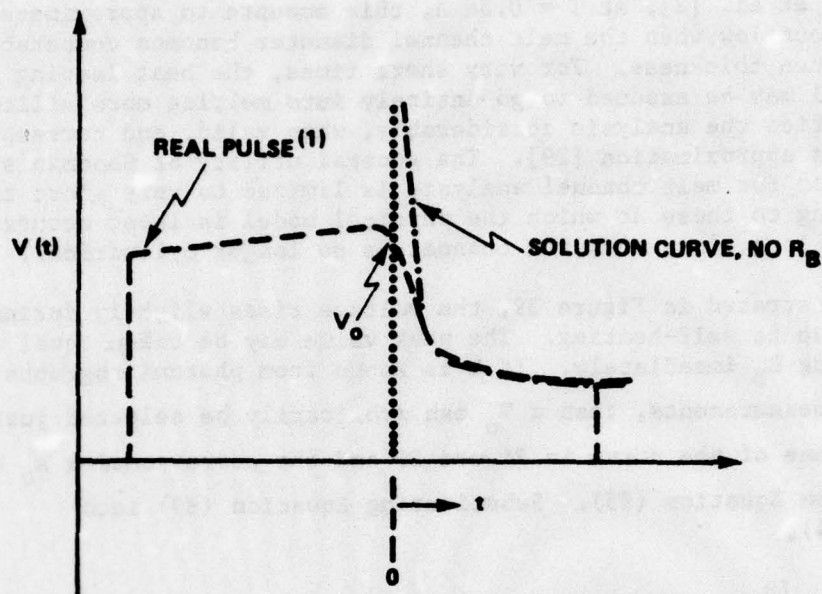


Figure 39. Junction voltage, entire pulse.

in conventional transistors must be handled on an individual basis, because such a variety of possibilities exists. It will be assumed that the solid-melt interface is perpendicular to the substrate (Figure 41).

For simplicity, constant (average) parameters will be assumed. Then, using rectangular coordinates,

$$c \rho_m \frac{\partial T}{\partial t} = K \frac{\partial^2 T}{\partial x^2} - H(T - T_m) + \vec{J} \cdot \vec{E} \quad (99)$$

in which T_m is the temperature at the bottom of the sapphire substrate. The new loss term can be removed by a change of variables, as discussed previously, or the equation can be solved directly. The latter will be done here.

For the purpose of illustrating the origin of this additional term, an average value K_{av} is assumed for the thermal conductivity and the generation term is temporarily ignored. As shown in Figure 41, the melt ribbon volume looks almost like a line source in comparison to the volume of the substrate. Then

$$Wd(q_x - q_{x+\Delta x}) = (q_d W_J W) \frac{\Delta x}{W_J} = q_d W \Delta x \quad (100)$$

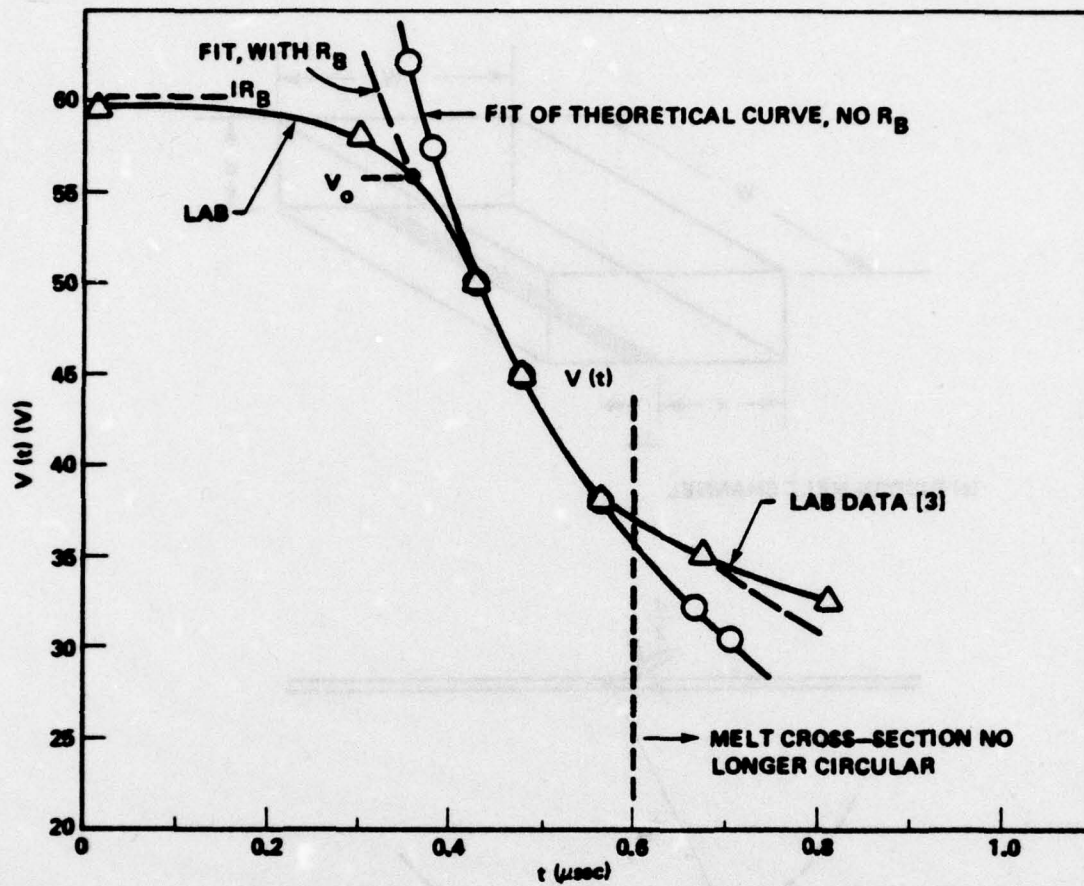


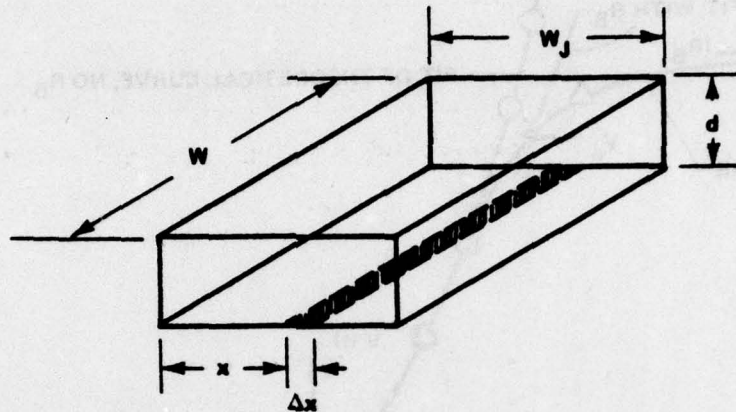
Figure 40. Comparison of theoretical and experimental voltages, falling portion of pulse.

or,

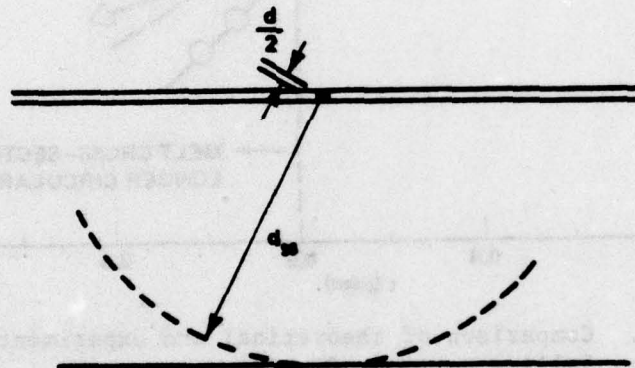
$$q_x - q_{x+\Delta x} = q_d \frac{\Delta x}{d} \quad (101)$$

Using Fourier's equation and taking the limit:

$$K_{av} \frac{d^2 T}{dx^2} = -\lim_{\Delta x \rightarrow 0} \left(\frac{\left. \frac{dT}{dx} \right|_x - \left. \frac{dT}{dx} \right|_{x+\Delta x}}{\Delta x} \right) = \frac{q_d}{d} \quad (102)$$



(a) RIBBON MELT CHANNEL



(b) SUBSTRATE AND "LINE SOURCE" (INTO PAGE)

Figure 41. Depletion region over substrate.

By making the (crude) assumptions that the temperature has reached ambient temperature T_∞ at a radius d_{ss} from the depletion region and that the melt region can be approximated by a cylinder of radius $d/2$, a rough approximation to q_d may be found. Within the substrate,

$$\nabla \cdot \vec{q}_d = \frac{1}{r} \frac{d}{dr} (r q_d) = 0 \quad (103)$$

Integrating and substituting Fourier's equation,

$$-rK_{ss} \frac{dT}{dr} - \frac{d}{2} q_d = 0 \quad (104)$$

In view of the approximations already made, an average thermal conductivity K_{ss} is assumed for the substrate. For sapphire, it is assumed that $K_{ss} = 0.15 \text{ W/cm}^\circ\text{K}$. Integrating a second time and using the boundary conditions described previously,

$$T - T_\infty = \frac{q_d d}{2K_{ss}} \ln \left(\frac{2d_{ss}}{d} \right) \quad (105)$$

or

$$q_d = \frac{2K_{ss}(T - T_\infty)}{d \ln \left(\frac{2d_{ss}}{d} \right)} \quad (106)$$

then,

$$K_{av} \frac{d^2 T}{dx^2} = \frac{q_d}{d} = \frac{2K_{ss}(T - T_\infty)}{d^2 \ln \left(\frac{2d_{ss}}{d} \right)} \equiv H(T - T_\infty) \quad (107)$$

Assuming $d = 1 \text{ } \mu\text{m}$, $d_{ss} = 250 \text{ } \mu\text{m}$, $K_{ss} = 0.15 \text{ W/cm}^\circ\text{K}$, the value of H to be used for this structure is $H = 5 \times 10^6 \text{ W/cm}^3\text{-}^\circ\text{K}$. As illustrated previously in Figure 37, the solid silicon around the melt channel quickly approaches the melt temperature. It thus appears that the temperature gradient within the melt channel always consists of a change of a very few degrees in a very short distance, while the late-time temperature gradient outside the ribbon-like channel consists of an equally small change in temperature across a much wider region. For this reason, Goodman's boundary approximation that all heat leaving the channel goes into melting becomes a fairly good approximation, unlike the situation at intermediate times. Goodman's approximation will be used here, because only the general trends are of interest. A more rigorous solution can be found by matching boundary velocities, as in the previous section. The equation for temperature outside the melt is replaced by a far more complicated one containing terms in

$$\text{erfc} \left(\frac{(x - s)}{\sqrt{4\alpha t}} \pm \sqrt{\frac{Ht}{c \rho_m}} \right) ;$$

no new information is gained.

The double moving boundary problem arising from growth in both the positive and negative x directions (Figure 42) can be simplified by a symmetry argument. A single boundary $s(t)$ is considered, where s is the distance from the centerline of the melt channel to the melt-solid interface, and current $I/2$ is used. The melt channel is L in length, $2s$ in width, and d in thickness. An "initial" square cross-section of side $s(t_0) = s_1 = d/2$ is assumed and the intrinsic channel resistance is ignored. Then

$$s = \frac{\sigma V^2}{c \rho_m L^2} = \frac{I^2}{4c \rho_m \sigma d^2 s^2} \quad (108)$$

$$V = \frac{IL}{2\sigma ds} \quad (109)$$

The boundary conditions given in Equations (68), (69), and (70) are still valid, provided r is replaced by x . If

$$T = T_m - a(s - x) + b(s - x)^2, \quad (110)$$

the coefficients are

$$a = \frac{\lambda}{2cs} \left[1 - \sqrt{1 + \frac{4cs^2}{\lambda} \left(s - \frac{4}{c\rho_m} [T_m - T_\infty] \right)} \right] \equiv \frac{v(s)}{s} \quad (111)$$

In less than 1 sec, the square root term goes to one (generation equals loss); the solution should not be carried beyond this point. Continuing,

$$b = \frac{a}{2s} = \frac{v}{2s^2} \quad (112)$$

Then, Equation (110) becomes

$$T = T_m - v \left(\frac{s - x}{s} \right) + \frac{v}{2} \left(\frac{s - x}{s} \right)^2 \quad (113)$$

$$\begin{aligned} \frac{ds}{dt} &= - \frac{\alpha c v(s)}{s\lambda} = - \frac{\alpha}{2s} \left[1 - \sqrt{1 + \frac{I^2}{\lambda \rho_m \sigma d^2} - \frac{4H(T_m - T_\infty)}{\lambda \rho_m} s^2} \right] \\ &= \left[\frac{\alpha}{4s} \frac{I^2}{\lambda \rho_m \sigma d^2} - \frac{4H(T_m - T_\infty)}{\lambda \rho_m} s^2 \right] \end{aligned} \quad (114)$$

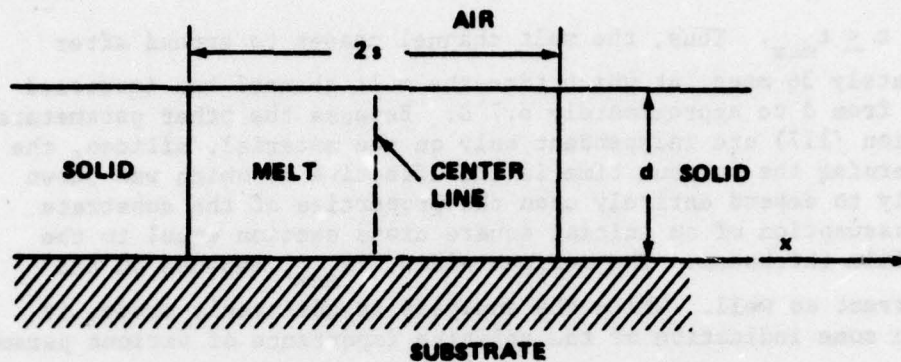


Figure 42. Cross section of melt channel in thin film diode.

Integrating,

$$s = \sqrt{s_{\max}^2 - (s_{\max}^2 - s_1^2) \exp \left\{ -\frac{2\alpha H}{\lambda \rho_m} (T_m - T_\infty)(t - t_1) \right\}}$$

$$= s_1 \sqrt{1 + \frac{2\alpha H(T_m - T_\infty)(s_{\max}^2 - s_1^2)}{\lambda \rho_m s_1^2} (t - t_1)} \quad (115)$$

where

$$s_{\max} = \frac{I}{2d \sqrt{\sigma H(T_m - T_\infty)}} \quad (116)$$

Squaring Equation (115) and letting $s = s_{\max}$,

$$t_{\max} = t_1 + \frac{\lambda \rho_m}{2\alpha H(T_m - T_\infty)} = \frac{\lambda \rho_m}{2\alpha H(T_m - T)} \quad (117)$$

Then

$$s = s_1 \sqrt{1 + \left(\frac{s_{\max}^2 - s_1^2}{s_1^2} \right) \left(\frac{t - t_1}{t_{\max} - t_1} \right)}$$

$$= \frac{1}{2} \sqrt{d^2 + \frac{2\alpha I^2}{\sigma \lambda \rho_m d^2} (t - t_1)} \quad (118)$$

for $t_1 \leq t \leq t_{\max}$. Thus, the melt channel ceases to expand after approximately 36 msec, at which time the melt channel has increased in width from d to approximately $6.7 d$. Because the other parameters in Equation (117) are independent only on the material, silicon, the term governing the maximum time is the effective H , which was shown previously to depend entirely upon the properties of the substrate and the assumption of an initial square cross section equal to the silicon film thickness. The maximum width, $2s_{\max}$, depends on the total current as well. While the analysis is admittedly crude, it does give some indication of the relative importance of various parameters. For example, if $\lambda = 9.17 \times 10^5$ J/kg is used (Table 3), t_{\max} is only 18 msec. Finally,

$$V = \frac{IL}{2\sigma ds} = \frac{V_1}{\sqrt{1 + \left(\frac{s_{\max}^2 - s_1^2}{s_1^2} \right) \left(\frac{t - t_1}{t_{\max} - t_1} \right)}} = \frac{V_1}{\sqrt{1 + \frac{4s_{\max}^2 (t - t_1)}{d^2 t_{\max}}}} \quad (119)$$

Equation (113), with the approximation for v given in Equation (114), can be used to demonstrate that for $I = 0.56$ A, the entire channel is essentially constant in temperature at T_m . This agrees with the trend begun in Figure 36. Figures 43 and 44 show $s(t)$ and $V(t)$, respectively. It is noted that Figure 40 ends at 1 μ sec and 32 V, while Figure 44 begins at 50 μ sec and 50 V. Thus, most of the activity occurs in less than 1 msec, with a very gradual decrease to a low voltage. If the test pulse is shorter than t_{\max} , the voltage drops with the fall time of the test pulse. There is really no effective way to show the entire pulse on a single graph; Figure 45 shows a composite of Figures 40 and 44 with a log-log scale. A third plateau exists at approximately 7.7 V and 36 msec, where the melt channel ceases to grow. The change in growth rate as the heat loss to the substrate becomes significant is clearly indicated. If the latent heat is only half as large as that used in the cancellations, the voltage at the tail of the pulse will effectively be divided by 1.4 and will drop somewhat more rapidly than indicated.

V. CURRENT MODE SECOND BREAKDOWN

Current mode second breakdown is a special form of breakdown occurring only in epitaxial planar transistors [4,31]. Because this construction process is so common, current mode second breakdown warrants special consideration. Moreover, under certain conditions, it can lead to thermal second breakdown and damage, even though in

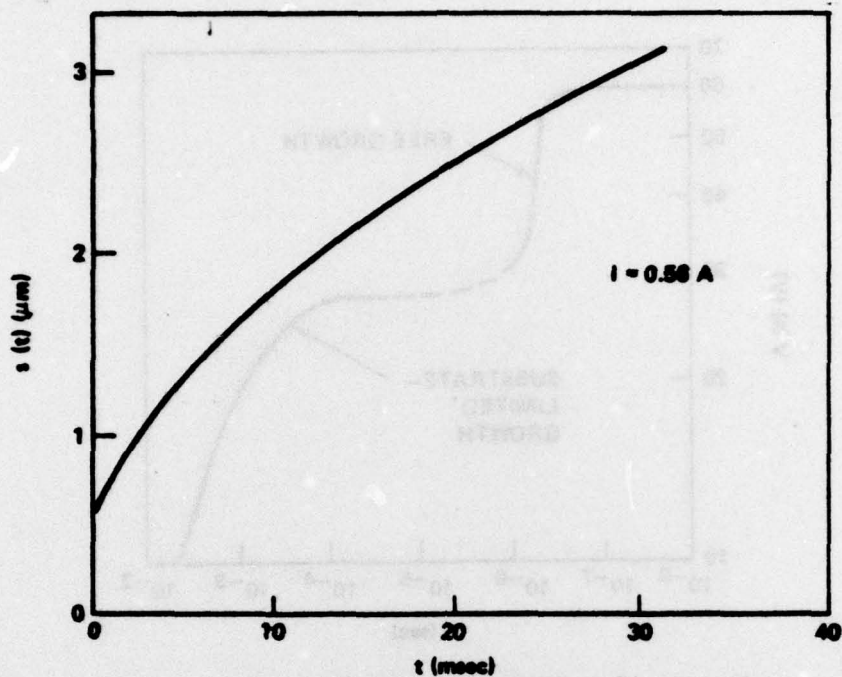


Figure 43. Channel half-width, long term.

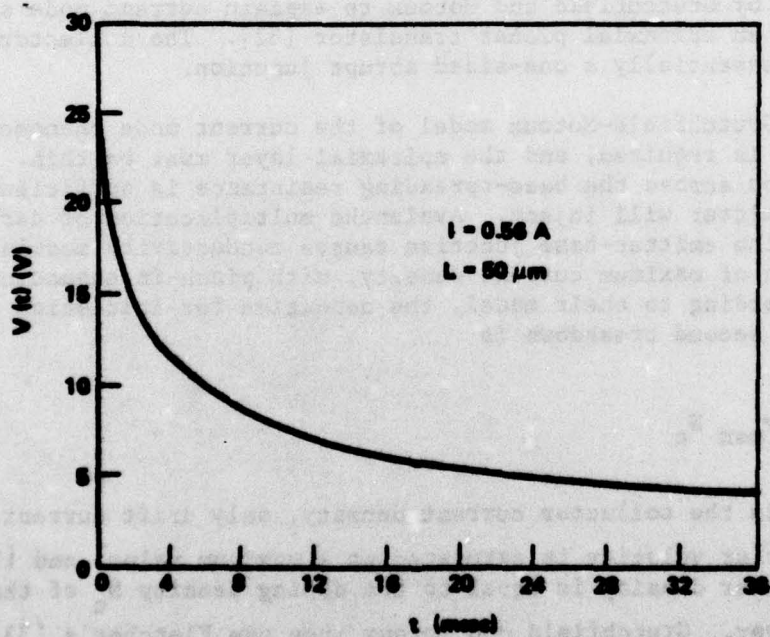


Figure 44. Voltage, long term.

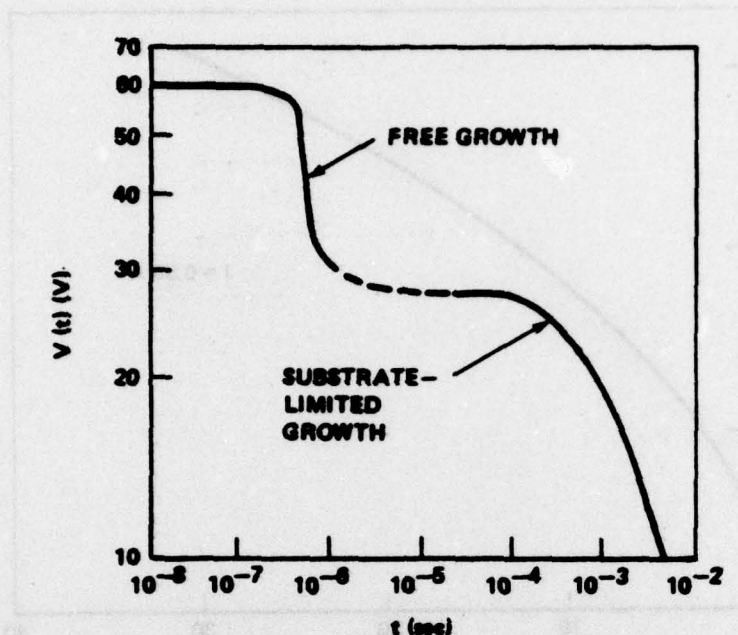


Figure 45. Composite voltage curve.

itself it is nondestructive [4]. Figure 46 shows the schematic cross-section used by Grutchfield and Motoux to explain current mode second breakdown in an epitaxial planar transistor [32]. The collector-base junction is essentially a one-sided abrupt junction.

In the Grutchfield-Motoux model of the current mode phenomenon, reachthrough is required, and the epitaxial layer must be thin. When the ohmic drop across the base-spreading resistance is sufficiently large, the emitter will inject. Avalanche multiplication of carriers injected by the emitter-base junction causes conductivity modulation in the region of maximum current density, with pinch-in enhancing the effect. According to their model, the condition for initiation of current mode second breakdown is

$$J_c = q v_{\max} N_c \quad (120)$$

in which J_c is the collector current density, only drift current is present, carrier velocity is saturated at a maximum value, and the majority carrier density is equal to the doping density N_c of the epitaxial layer. Grutchfield and Motoux then use Fletcher's [33] solution for the current density at a distance r from the center of the emitter:

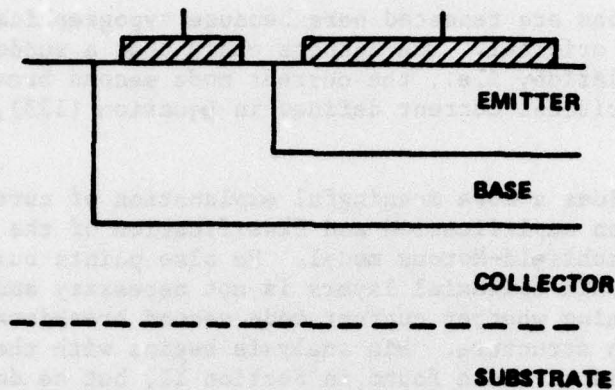


Figure 46. Schematic of epitaxial planar transistor, cross-sectional view.

$$J_E(r) = \frac{J_{E1}}{[1 - a(r_E - r)]^2} \quad (121)$$

in which

$$a = \sqrt{\frac{q}{2kT} \frac{(\alpha_f M - 1)}{\sigma_B W_B} J_E} \quad (122)$$

where

r_E = radius of emitter

J_{E1} = current density at r_E

α_f = large-signal common base current gain

σ_B = base conductivity

W_B = base width

J_E = average current density in emitter

and integrate to get emitter current I_E required to initiate current mode second breakdown:

$$I_E = \int_0^{r_E} 2\pi r J_E(r) dr = \frac{1}{a^2} \left[\ln \left(\frac{1}{1 - ar_E} \right) - ar_E \right] \quad (123)$$

The preceding equations are repeated here because typographical errors appear in the original. The authors claim that a sudden change in conductivity modulation, i.e., the current mode second breakdown, takes place at the critical current defined in Equation (123), but they do not say why.

Raburn [4] provides a more meaningful explanation of current mode second breakdown by an amplification and clarification of the ideas expressed in the Grutchfield-Motoux model. He also points out that their limitation to thin epitaxial layers is not necessary and lists criteria for determining whether current mode second breakdown will take place in a given structure. His analysis begins with the same differential equations as those found in Section II, but he does not neglect mobile carriers in Poisson's equation (shown here for cartesian coordinates):

$$\frac{d}{dx} = \frac{1}{\epsilon} \left(qN + \frac{J_p}{v_{lp}} - \frac{J_n}{v_{ln}} \right) \quad (124)$$

in which the mobile carriers are assumed to be flowing only by drift and at their saturation velocities:

$$J_p = q p v_{lp} \quad (125)$$

$$J_n = q n v_{ln} \quad (126)$$

An injection ratio,

$$\gamma = \frac{J_p(W)}{J} \quad , \quad (127)$$

is defined and results explained in terms of it. Figures 47, 48, and 49 show electric field variation across the depletion region for a one-sided abrupt collector-base junction at reachthrough and $\gamma = 0.1$, 0.5, and 1 [4]. The distribution is seen to vary greatly at higher values of J .

The following is a brief sketch of the Raburn model. An emitter configuration at reachthrough is considered. As current through the base increases, the voltage across the base spreading resistance will eventually reach the avalanche breakdown voltage of the emitter-base junction. This will occur first near the top surface of the chip. Once current flows through the avalanching region, it can proceed down-ward to the planar central portion of the emitter-base junction depletion region (which will be forward biased), where it will be

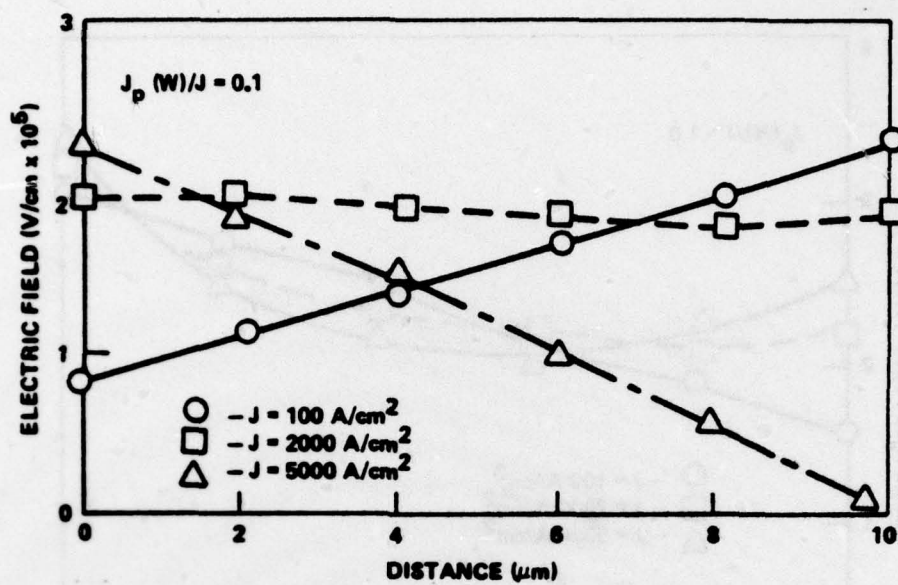


Figure 47. Field distribution for $\gamma = 0.1$ [4].

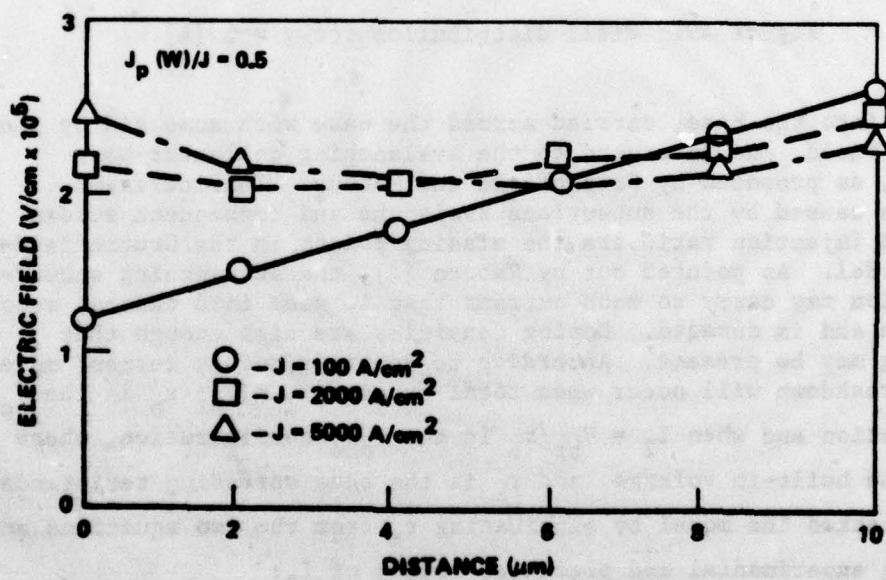


Figure 48. Field distribution for $\gamma = 0.5$ [4].

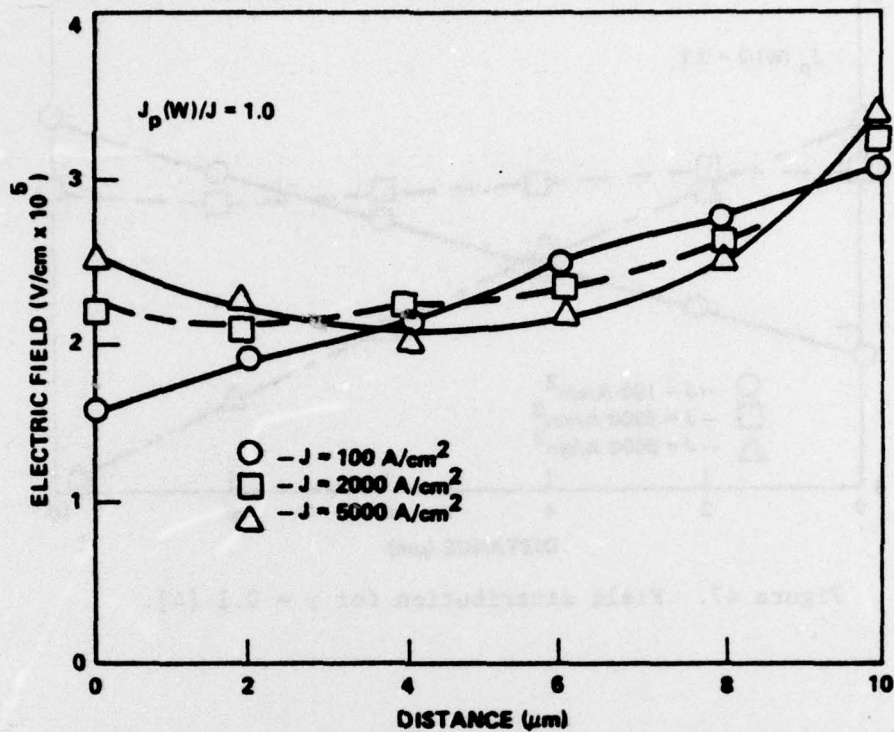


Figure 49. Field distribution for $\gamma = 1$ [4].

injected into the base, carried across the base with some aid by the built-in field, and go onward to the avalanching collector-base junction, as proposed by Grutchfield and Motoux. The increased injection caused by the subsurface avalanche and consequent sudden change in injection ratio are the missing points in the Grutchfield-Motoux model. As pointed out by Raburn [4], the avalanching subsurface region may carry so much current that it goes into thermal second breakdown and is damaged. Doping densities are high enough that tunneling may be present. According to Raburn's model, current mode second breakdown will occur when total current $I_1 = V_{bi}/r_b$ in the V_{cer} configuration and when $I_2 = V_{br}/r_b$ in the V_{cbo} configuration, where V_{bi} is the built-in voltage, and r_b is the base spreading resistance. Raburn checked the model by eliminating r_b from the two equations and comparing experimental and predicted values of I_2 :

$$I_2 = \frac{V_{br}}{V_{bi}} I_1 \quad (128)$$

Because $I_2 = 20 I_1$, the value of r_b could not be expected to remain completely constant; nevertheless, the results were in reasonably good agreement.

It may be possible to extend the analysis somewhat by replacing the base-spreading resistance with a junction field effect transistor (JFET) as illustrated in Figure 50. Diode D_1 represents the avalanching subsurface region, and diode D_3 represents the collector in reach-through, so avalanche diodes ("Zeners") are used in the equivalent circuit. Diode D_2 is an ordinary forward-biased diode, and R_{ss} is the substrate resistance. Each symbol represents a nonideal, lumped element; resistances, capacitances, etc. are not shown explicitly. Standard JFET analysis may yield a much better expression for the nonlinear base spreading resistance. It should be noted that Figure 45 is somewhat misleading in that it does not warn that a ring-dot geometry is involved and that the effective source-drain current flows radially in a cylinder.

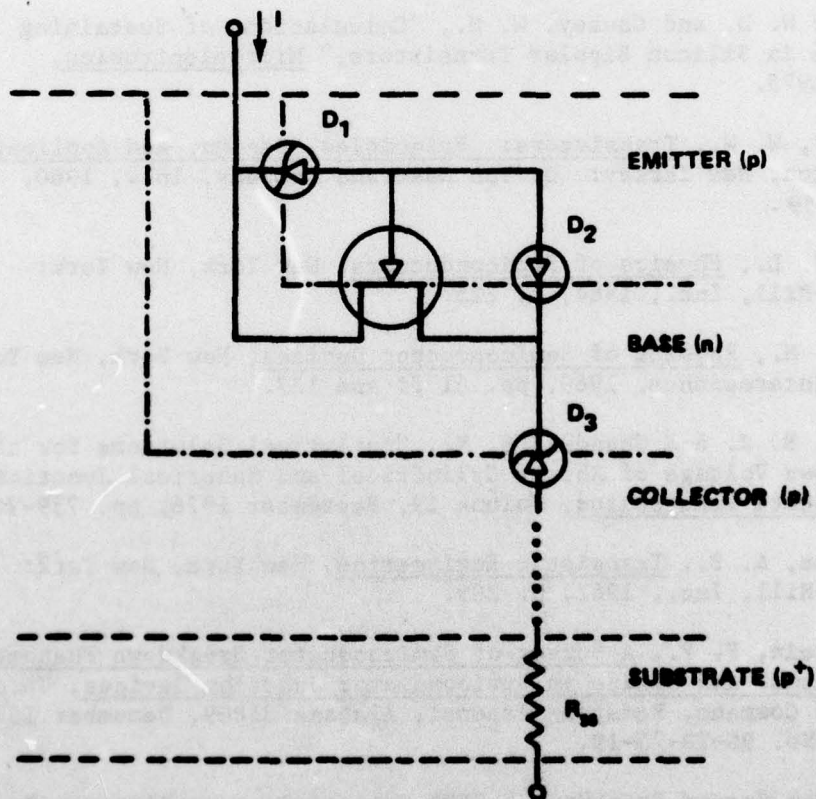


Figure 50. Equivalent circuit with nonideal lumped elements (pnnp).

REFERENCES

1. Raburn, W. D. and Mathews, D., "Geometric and Doping Effects on Avalanche and Sustaining Voltages in Transistors," 1977 IEEE Region 3 Conference, Williamsburg, Virginia, April 4-6, 1977.
2. Budenstein, P. P., Pontius, D. H., and Smith, W. B., Second Breakdown and Damage in Semiconductor Junction Devices, US Army Missile Command, Redstone Arsenal, Alabama 35802, April 1972, Report No. RG-TR-72-15 (AD-740226).
3. Grove, A. S., Leistiko, Jr., O., and Hooper, W. W., "Effect of Surface Fields on the Breakdown Voltage of Planar Silicon p-n Junctions," IEEE Transactions on Electron Devices, Volume ED-14, No. 3, March 1967, pp. 157-162.
4. Raburn, W. D., An Investigation of Current Mode Second Breakdown, Bureau of Engineering Research, University of Alabama, University, Alabama, July 1974, Report No. 177-93.
5. Raburn, W. D. and Causey, W. H., "Calculations of Sustaining Voltage in Silicon Bipolar Transistors," Microelectronics, March 1975.
6. "Gartner, W. W., Transistors: Principles, Design, and Applications, Princeton, New Jersey: D. Van Nostrand Company, Inc., 1960, pp. 55-59.
7. Moll, J. L., Physics of Semiconductors, New York, New York: McGraw-Hill, Inc., 1964, p. 225.
8. Sze, S. M., Physics of Semiconductor Devices, New York, New York: Wiley-Interscience, 1969, pp. 61 ff and 127.
9. Baliga, B. J. and Ghandhi, S. K., "Analytical Solutions for the Breakdown Voltage of Abrupt Cylindrical and Spherical Junctions," Solid State Electronics, Volume 19, September 1976, pp. 739-744.
10. Phillips, A. B., Transistor Engineering, New York, New York: McGraw-Hill, Inc., 1962, p. 209.
11. Budenstein, P. P., A Survey of Semiconductor Breakdown Phenomena, Mechanisms, and Damage in Semiconductor Junction Devices, US Army Missile Command, Redstone Arsenal, Alabama 35809, December 1970, Report No. RG-TR-70-19.
12. "Issue on Second Breakdown," IEEE Transactions on Electron Devices, Volume ED-13, November 1966.

13. "Special Issue on Second Breakdown," IEEE Transactions on Electron Devices, Volume ED-13, August/September 1966.
14. Ward, A. L., "An Electro-Thermal Model of Second Breakdown," IEEE Transactions on Nuclear Science, Volume NS-23, No. 6, December 1976, pp. 1679-1684.
15. Sutherland, A. D. and Kennedy, D. P., "A Computer Model for Lateral Thermal Instabilities in Power Transistors," Transactions of International Electron Device Meeting, Washington, D.C., December 1975, p. 569.
16. Raburn, W. D. and Causey, W. H., Determination of Semiconductor Junction Vulnerability to Second Breakdown, Bureau of Engineering Research, University of Alabama, University, Alabama, July 1975, Report No. 200-93.
17. Causey, W. H. and Raburn, W. D., "A Numerical Model for Thermal Second Breakdown in Diodes," 1977 IEEE Region 3 Conference, Williamsburg, Virginia, April 4-6, 1977.
18. Ford, G. M., "Collector-to-Emitter Breakdown Related to Thermal Runaway in Homogeneous-Base Germanium Power Transistors," Solid State Design, Volume 4, June 1963, pp. 29-36.
19. Melchior, H. and Strutt, M. J. O., "Secondary Breakdown in Transistors," Proceedings of the IEEE, Volume 52, April 1964, pp. 439-440.
20. Schafft, H. A. and French, J. C., "Second Breakdown in Transistors," IRE Transactions on Electron Devices, Volume ED-9, March 1962, pp. 129-136.
21. Wunsch, D. C. and Bell, R. R., "Determination of Threshold Failure Levels of Semiconductor Diodes and Transistors Due to Pulse Voltages," IEEE Transactions on Nuclear Science, Volume NS-15, December 1968, pp. 244-259.
22. Sunshine, R. A., Avalanching and Second Breakdown in Silicon-on-Sapphire Diodes, RCA Laboratories, Princeton, New Jersey, 1970, Technical Report PRRL-70-TR-245.
23. Dumin, D. J., "Emission of Visible Radiation from Extended Plasma in Silicon Diodes During Second Breakdown," IEEE Transactions on Electron Devices, Volume ED-9, March 1962, pp. 129-136.
24. Pontius, D. H., Smith, W. B., Baruah, A., and Budenstein, P. P., Second Breakdown in the Presence of Intense Ionizing Radiation, US Army Missile Command, Redstone Arsenal, Alabama 35802, December 1974, Report No. RG-TR-75-24.

25. English, A. C., "Mesoplasma and 'Second Breakdown' in Silicon Junctions," Solid State Electronics, Volume 6, September 1963, pp. 511-521.
26. Navon, D. H., "Power Transistor Stability and Reliability," Interim Technical Report on Contract No. DAAB-07-71-C-0260, September 1972.
27. Berglund, C. N. and Klein, N., "Thermal Effects on Switching of Solids from an Insulating to a Conductive State," Proceedings of the IEEE, Volume 59, No. 7, July 1971, pp. 1099-1109.
28. English, A. C., "Physical Investigation of the Mesoplasma in Silicon," IEEE Transactions on Electron Devices, Volume ED-13, August 1966, pp. 662-667.
29. Goodman, T. R., "The Heat-Balance Integral and Its Application to Problems Involving a Change of Phase," Transactions of the ASME, Volume 80, 1958, pp. 335-342.
30. Finlayson, B. A., The Method of Weighted Residuals and Variational Principles, New York, New York: Academic Press, 1972.
31. Abramowitz, M. and Stegun, I. A., Handbook of Mathematical Functions, Washington, D.C.: National Bureau of Standards, US Government Printing Office, June 1964, p. 231.
32. Grutchfield, H. B. and Motoux, T. J., "Current Mode Second Breakdown in Epitaxial Planar Transistors," IEEE Transactions on Electron Devices, Volume ED-13, November 1966, pp. 743-748.
33. Fletcher, N. A., "Some Aspects of the Design of Power Transistors," Proceedings of the IRE, Volume 43, May 1955, pp. 551-559.

DISTRIBUTION

	No. of		No. of
Director Advanced Research Projects Agency Architect Building Attn: Director, Strategic Technology Office Arlington, Virginia 22209	1	Director Advanced Ballistic Missile Defense Agency Commonwealth Building 1320 Wilson Boulevard Arlington, Virginia 22209	1
Assistant to the Secretary of Defense (Atomic Energy) Attn: Document Control Washington, D. C. 20301	1	Commander Army Air Defense Board Attn: Security Officer Fort Bliss, Texas 79916	1
Commander Continental Air Defense Command Attn: DCS/C&E (CESA) Ent Air Force Base Colorado Springs, Colorado 80912	1	Commander Army Airborne Electronics and Special Warfare Board Attn: Library Fort Bragg, North Carolina 29307	1
Director Defense Nuclear Library Attn: APTL, (Technical Library) ARSI (Archives) RAEV Washington, D. C. 20305	2 1 1	Chief Army Communications Systems Agency Attn: Library Fort Monmouth, New Jersey 07703	1
Director Defense Communications Agency Attn: Code 340 Washington, D. C. 20305	1	Commander Army Electronic Proving Ground Attn: STEPP-PA-I Fort Huachuca, Arizona 85613	1
Defense Documentation Center Cameron Station Alexandria, Virginia 22314	2	Commander Army Electronics Command Missile Electronic Warfare Technical Area Attn: Chief, Special Projects Team White Sands Missile Range, New Mexico 88002	1
Director Defense Intelligence Agency Attn: DIAST-3, Weapons and Systems Office DIAST-88, Phys. Vulnerability Division Washington, D. C. 20301	1 1	Commander Army Mobility Equipment Research and Development Center Attn: SMEFB-EAX Fort Belvoir, Virginia 22060	1
Director of Defense Research and Engineering Attn: Assistant Director (Research), Washington, D. C. 20301	1	Commander Army Ordnance Center and School Attn: Library Aberdeen Proving Ground, Maryland 21005	1
Chairman Joint Chiefs of Staff Attn: J-6, Communications and Electronics Washington, D. C. 20301	1	Chief Army Satellite Communications Agency Attn: DMCPM-SC-6 Fort Monmouth, New Jersey 07703	
Director Joint Strategic Target Planning Staff Attn: Document Control Officer Offutt Air Force Base Omaha, Nebraska 68113	1	Commander Army Signal Center and School Building 1207 Attn: Librarian Fort Monmouth, New Jersey 07703	
Commander, Test Command Defense Nuclear Agency Attn: TCDF Sandia Base Albuquerque, New Mexico 87115	1	Department of the Army Assistant Chief of Staff for Communications-Electronics Attn: CEO Washington, D. C. 20314	
Director Weapons Systems Evaluation Group, ODURAE Office, Secretary of Defense Attn: Technical Information Branch 400 Army-Navy Drive Washington, D. C. 20305	1	Department of the Army Assistant Chief of Staff for Force Development Attn: Director of Chemical and Nuclear Operations Washington, D. C. 20310	1
		Director Ballistic Research Laboratories Attn: Technical Library Aberdeen Proving Ground, Maryland 21005	1

	No. of Copies		No. of Copies
Department of the Army Chief of Engineers Attn: ENGMC-DE -ED Washington, D. C. 20314	1 1	Commander US Army Foreign Science and Technology Center Attn: Research and Data Branch 220 7th Street NE Charlottesville, Virginia 22901	1
Department of the Army Chief of Research and Development Attn: NCB Div ARMDA-00 Washington, D. C. 20310	1 1	Commander US Army Materiel Command Attn: Director of Development 5001 Eisenhower Avenue Alexandria, Virginia 22333	1
Department of the Army Director of Civil Defense Attn: RE(SS) Washington, D. C. 20310	1	Commander US Army Munitions Command Attn: DRSMU-QA -RE-RT Picatinny Arsenal Dover, New Jersey 07801	1 1
Department of the Army Harry Diamond Laboratories Attn: Technical Reference Branch DRXDO-NP: Branch 0027, -RB: Branch 270 Branch 280 DRXDO-EM: Branch 1000 Branch 1010, Branch 1020 Nuclear Weapons Effects Projects Office Washington, D. C. 20438	1 1 1 1 1 1	Commander US Army Strategic Communications Command Attn: SCCX-SSA-OD -CNO Fort Huachuca, Arizona 85613	1 1
Commander Attn: SMUPA-TW -WC -TW Picatinny Arsenal Dover, New Jersey 07801	1 1 1	Commander US Continental Army Command Attn: ATOPS-ING-TSM Fort Monroe, Virginia 23351	1
Commander Safeguard System Command Attn: SAFSC-STP P. O. Box 1500 Huntsville, Alabama 35807	1	Commander Attn: STEWS-AD-L (Technical Library) -TE-N (Nuclear Wpns. Effect Lab.) White Sands Missile Range, New Mexico 88002	1
Commander Safeguard Systems Evaluation Agency Attn: SAFSEA-EA-T White Sands Missile Range New Mexico 88002	1	Department of the Navy Chief of Naval Research Attn: Code 418 Arlington, Virginia 22217	1
Director US Army Advanced Ballistic Missile Defense Agency Huntsville Office Attn: CRDAM-X P. O. Box 1500 Huntsville, Alabama 35807	1	Commander Naval Electronics Laboratory Center Attn: Technical Library San Diego, California 92152	1
Commander US Army Combat Developments Command Air Defense Agency Attn: Document Control Fort Bliss, Texas 79916	1	Commander Naval Ordnance Laboratory Attn: 1-314, Technical Library Code 431 Silver Springs, Maryland 20910	1 1
Commander US Army Electronics Command Attn: DRHEL-CD-TC -HL-D -ED-P -KL-I -EL-D -CT-D -KL-I Fort Monmouth, New Jersey 07703	1 1 1 1 1 1 1	Superintendent Naval Postgraduate School Attn: Code 2124, Technical Reports Librarian Monterey, California 93940	1
		Director Naval Research Laboratory Attn: Code 7750 Code 6465 Code 5000 Washington, D. C. 20390	1 1
		Commander Naval Weapons Evaluation Facility Attn: Document Control Kirtland Air Force Base Albuquerque, New Mexico 87117	1

	No. of Copies		No. of Copies
AF Cambridge Research Laboratories, AFSC		Sandia Laboratories	
Attn: CROR	1	Attn: Document Control for:	
CEWII,	1	ORG. 5100	1
L. G. Hanscom Field		P. O. Box 5800	
Bedford, Massachusetts 01730		Albuquerque, New Mexico 87115	
AF Institute of Technology, AU		US Atomic Energy Commission	
Attn: Library, AFIT (LD)	1	Albuquerque Operations Office	
Building 640, Area B		Attn: Document Control	1
Wright-Patterson Air Force Base,		P. O. Box 5400	
Ohio 54533		Albuquerque, New Mexico 87115	
Commander		University of California	
AF Special Weapons Center, AFSC		Lawrence Radiation Laboratory	
Attn: SWVT	1	Technical Information Division	
SWTSX, Survivability	1	P. O. Box 808	
Vulnerability Branch	1	Livermore, California 94550	
Kirtland Air Force Base,		Aerospace Corporation	
New Mexico 87117		Attn: Weapons Effects Department	1
AF Weapons Laboratory AFSC		P. O. Box 5866	
Attn: Chief, EST	1	San Bernardino, California 92408	
Kirtland Air Force Base,		Aerospace Corporation	
New Mexico 87117		Attn: Library	1
Air Force Avionics Laboratory, AFSC		P. O. Box 95085	
Attn: AFAL (AVO-2), Stinfo Office	1	Los Angeles, California 90045	
Wright-Patterson Air Force Base		AVCO	
Ohio 45433		Government Products Group	
Director Air Force Office of Scientific		Attn: Research Library, A830	1
Research		Room 2201	
Office of Aerospace Research		201 Lowell Street	
Attn: SRGC	1	Wilmington, Massachusetts 01887	
1400 Wilson Boulevard		Bell Telephone Laboratories, Inc.	
Arlington, Virginia 22209		Mountain Avenue	
Commander		Murray Hill, New Jersey 07971	
Air Force Systems Command		Braddock, Dunn and McDonald, Inc.	
Attn: DLSP (General Physics)	1	P. O. Box 10694	
Andrews Air Force Base		El Paso, Texas 79997	
Washington, D. C. 20331		Braddock, Dunn and McDonald, Inc.	
Commander		8027 Leesburg Pike	
Electronic Systems Division, AFSC		McLean, Virginia 22101	1
Attn: ESSXS (NEWS Proj. Off.)	1	Dikewood Corporation	
L. G. Hanscom Field		University Research Park	
Bedford, Massachusetts 01730		1009 Bradbury Drive, SE	
Commander		Albuquerque, New Mexico 87106	1
Foreign Technology Division, AFSC	1	EG&G, Inc.	
Attn: TD-STA, Library	1	P. O. Box 4339	
TDFTM	1	Albuquerque, New Mexico 87106	1
Wright-Patterson Air Force Base		EG&G, Inc.	
Ohio 45433		Attn: Document Control Center	1
Commander		P. O. Box 227	
Rome Air Development Center, AFSC		Bedford, Massachusetts 01730	
Attn: ENTLD, Documents Library		General Electric Company	
Griffiss Air Force Base, New York 13440		Tempo-Center for Advanced Studies	
US Atomic Energy Commission		Attn: DASA Information and	
Assistant General Manager for		Analysis Center	1
Military Application		816 State Street	
Attn: Document Control for	1	Santa Barbara, California 93102	
Research and Development Branch		General Research Corporation	
Washington, D. C. 20545		Attn: Technical Information Office	1
Los Alamos Scientific Laboratory		P. O. Box 3587	
Attn: Technical Library	1	Santa Barbara, California 93105	
P. O. Box 1663			
Los Alamos, New Mexico 87544			

	No. of Copies		No. of Copies
IIT Research Institute Attn: Assist. Dir of Research 10 West 35th Street Chicago, Illinois 60616	1	Systems, Science and Software, Inc. P. O. Box 1620 La Jolla, California 92037	1
Institute for Defense Analyses 400 Army-Navy Drive Arlington, Virginia 22202	1	TRW Systems Group One Space Park Attn: Technical Information Center/S-1930 Redondo Beach, California 90278	1
Kaman Sciences Corporation Kaman Nuclear Division 1700 Garden of the Gods Road Colorado Springs, Colorado 80907		Superior Technical Services, Inc. Attn: T. Ward 4308 Governors Drive Huntsville, Alabama 35805	1
Martin Marietta Aerospace Orlando Division Attn: Engineering Library P. O. Box 3837 Orlando, Florida 32805	1	DRSMT-LP, Mr. Voigt	1
Martin Marietta Corporation Denver Division Attn: Research Library P. O. Box 179 Denver, Colorado 80201	1	DRDWT-X	1
Maxwell Laboratories, Inc. 9244 Balboa Avenue San Diego, California 92123		-T, Dr. Kobler	1
McDonnell Douglas Corporation Attn: AZ-260 Library 3855 Lakewood Boulevard Long Beach, California 90801		-EA	1
Mission Research Corporation 812 Anacapa Street Santa Barbara, California 93101		-TR	1
North American Rockwell Corporation Automotives Division 3370 Miraloma Avenue Anaheim, California 92803		-TK	1
Physics International Company Attn: Document Control 2700 Merced Street San Leandro, California 94577	1	-TE	1
Rand Corporation 1700 Main Street Santa Monica, California 90406		-TL	1
Research Analysis Corporation Attn: Document Library McLean, Virginia 22101	1	-ET	1
Stanford Research Institute 4810 Bradford Boulevard, N. W. Huntsville, Alabama 35805		-TG	1
Commander Army Nuclear Weapons Study Group Attn: Library Fort Belvoir, Virginia 22060	1	-TGX	1
Stanford Research Institute 333 Ravenswood Avenue Menlo Park, California 94025	1	-TGG	1
		-TGC	1
		-TCN	1
		-TCL	1
		-TGI	1
		-EAA	20
		-TBD	3
		-TI (Record Set)	1
		(Reference Copy)	1